Geophysical Research Letters

28 JULY 2010
Volume 37 Number 14
AGU American Geophysical Union

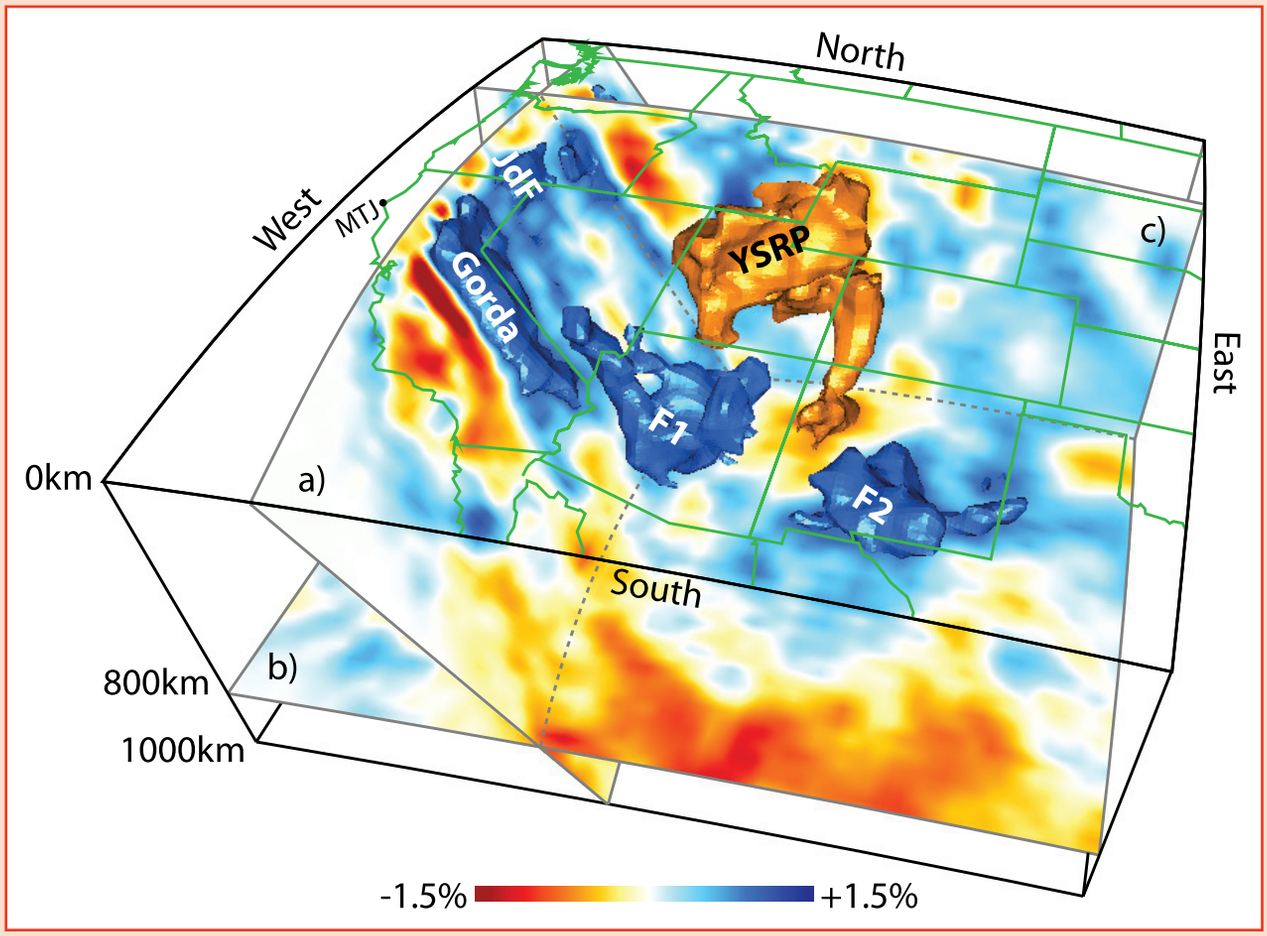

Slab-plume interaction beneath the Pacific Northwest • Changes in Sun's plasma conveyor belt affect solar cycle • Convergence of El Niño and NAO brings heavy snowfall • South America exposed to increased ultraviolet light

GEOPHYSICAL RESEARCH LETTERS, VOL. 37, L14305, doi:10.1029/2010GL043489, 2010

Slab-plume interaction beneath the Pacific Northwest

Mathias Obrebski,[1] Richard M. Allen,[1] Mei Xue,[2] and Shu-Huei Hung[3]

Received 1 April 2010; revised 4 June 2010; accepted 16 June 2010; published 22 July 2010.

[1] The Pacific Northwest has undergone complex plate reorganization and intense tectono-volcanic activity to the east during the Cenozoic (last 65 Ma). Here we show new high-resolution tomographic images obtained using shear and compressional data from the ongoing USArray deployment that demonstrate first that there is a continuous, whole-mantle plume beneath the Yellowstone Snake River Plain (YSRP) and second, that the subducting Juan de Fuca (JdF) slab is fragmented and even absent beneath Oregon. The analysis of the geometry of our tomographic models suggests that the arrival and emplacement of the large Yellowstone plume had a substantial impact on the nearby Cascadia subduction zone, promoting the tearing and weakening of the JdF slab. This interpretation also explains several intriguing geophysical properties of the Cascadia trench that contrast with most other subduction zones, such as the absence of deep seismicity and the trench-normal fast direction of mantle anisotropy. The DNA velocity models are available for download and slicing at http://dna.berkeley.edu. **Citation:** Obrebski, M., R. M. Allen, M. Xue, and S.-H. Hung (2010), Slab-plume interaction beneath the Pacific Northwest, *Geophys. Res. Lett.*, *37*, L14305, doi:10.1029/2010GL043489.

1. Introduction

[2] The Pacific Northwest of western North America is unusual in that both a subducting slab and a hotspot occur within ~1000 km of one another. Globally, these geologic components are commonly separated into distinct provinces [*Davaille et al.*, 2005]. The Juan de Fuca plate that continues to subduct today (Figure 1) is a remnant corner of the Farallon plate and is terminated to the south by the Mendocino Triple Junction (MTJ). Subduction beneath the Pacific Northwest has been continuous for more than ~150 Ma [*Severinghaus and Atwater*, 1990; *Bunge and Grand*, 2000]. The westernmost US exhibits several major Neogene to Quaternary volcanic provinces. The Columbia River Basalts (CRB, Figure 1) is the product of a phase of massive volcanic outpouring that occurred ~17 Ma. The Yellowstone Snake River Plain (YSRP) hosts a bimodal volcanic trend that exhibits a time progressive sequence of volcanic centers (Figure 1). Two groups of hypotheses have been proposed to explain this surface geology: a stationary deep-seated whole mantle plume [*Morgan*, 1971; *Pierce and Morgan*, 1992; *Pierce et al.*, 2000; *Camp and Ross*, 2004; *Waite et al.*, 2006; *Smith et al.* 2009], or various lithospheric-driven processes of fracture and volcanism [*Dickinson*, 1997; *Humphreys et al.*, 2000; *Christiansen et al.*, 2002]. Nevertheless, seismic imaging efforts to constrain the geometry of any Yellowstone plume anomaly through the mantle have been inconclusive. Here we take advantage of the Yellowstone region being now well covered by the dense USAarray deployment to provide constraints on the source of the hotspot, the process of subduction, and the inevitable interaction between the two in the mantle beneath the Pacific Northwest.

2. Data and Method

[3] To image the earth's interior beneath the Pacific Northwest, we use all of the available Earthscope-USArray data recorded from January 2006 to July 2009 (Figure S1 of the auxiliary material).[4] The station coverage extends from the west coast to ~100°W and from the Mexican to the Canadian boarder. We also processed the data from two Earthscope temporary arrays (FACES and Mendocino Experiment) deployed along the Cascadia trench and permanent seismic networks in the western US, enhancing the resolution achieved for this region. The velocity structure of the mantle is retrieved through body wave finite frequency tomographic inversion. The dataset of our multi-frequency compressional model DNA09-P is derived from 58,670 traveltimes of direct P from 127 earthquakes measured in four frequency bands. The dataset used for our shear model DNA09-S includes 38,750 travel-time measurements, 34,850 S-wave observations from 142 events and 3,900 SKS observations from 24 events (see auxiliary material).

3. Results

[4] The structures displayed in our P- and S-wave models are consistent despite the difference in the wavelengths of the signals used (Figure S2). Checkerboard resolution tests show good recovery beneath the seismic array to a depth of 1200 km (Figures S3–S6) and we also performed specifically designed resolution tests to demonstrate the robustness of the features described below (Figures S7–S10). Aside from specific cases discussed in the next sections, our two models are in good agreement (see auxiliary material) with previous USAarray based models [*Roth et al.*, 2008; *Sigloch et al.*, 2008; *Burdick et al.*, 2009].

3.1. Juan de Fuca Slab

[5] The north-south elongated fast anomaly associated with the JdF slab is clearly imaged in our P- and S-wave models (Figures 2a and S2). At 200 km depth, its signature is strong (up to 2%) in Northern California and Washington, and weak in Oregon (less than 1%). The strong-to-weak fast

[1]Department of Earth and Planetary Science, University of California, Berkeley, California, USA.
[2]School of Ocean and Earth Science, Tongji University, Shanghai, China.
[3]Department of Geosciences, National Taiwan University, Taipei, Taiwan.

0094-8276/10/2010GL043489

[4]Auxiliary materials are available in the HTML. doi:10.1029/2010GL043489.

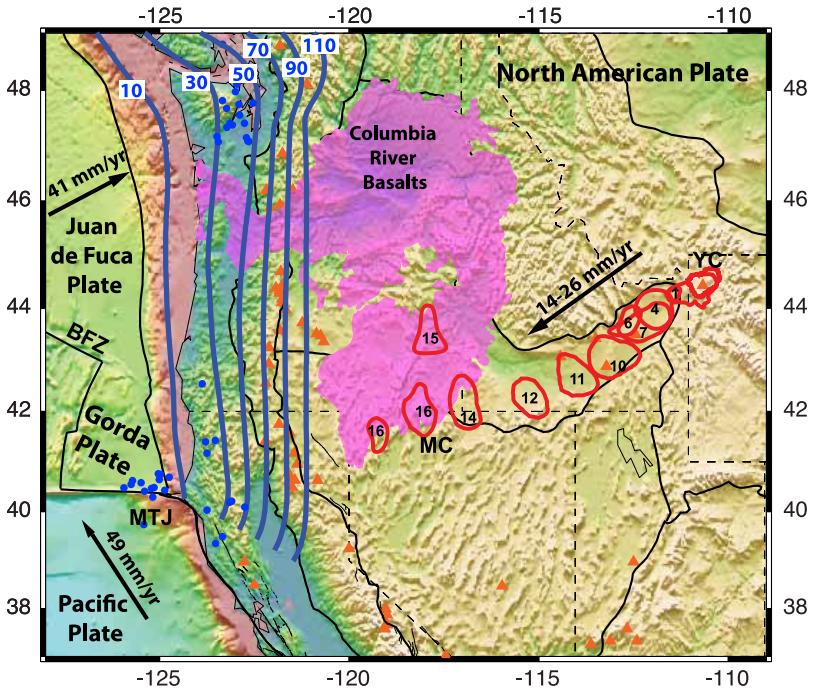

Figure 1. Geologic-tectonic features of the Pacific Northwest of the United States overlaid on topography and bathymetry. North from the Mendocino Triple Junction (MTJ), the Gorda and JdF plates, separated by the Blanco Fracture Zone (BFZ), are subducting beneath the North American plate with an oblique convergence rate of 41 mm/yr. The estimated depth of the top of subducting slab is shown with blue contours labelled in km. The location of all M > 4 earthquakes with depth ≥35 km since 1970 are shown as blue dots. Volcanoes are shown as orange triangles. The Yellowstone Hotspot Track exhibits a series of time-progressive regions of caldera-forming eruptions (red outline) from McDermitt (MC) to the currently active Yellowstone Caldera (YC). The track is approximately parallel to the absolute plate motion of North America, which is estimated to be 14–26 mm/yr to the southwest. Numbers indicate the age of the calderas (in Ma). The Columbia River Flood Basalt Province was a massive outpouring of basalt from ~16.6 to ~15.0 Ma and is shown in pink [*Camp and Ross*, 2004].

anomaly transition in southern Cascadia coincides with the Blanco Fracture Zone that divides the Gorda and JdF sections of the slab (Figures 1 and 2a). Figures 2 and 3 show that the slab is surprisingly short compared to the several thousand kilometers of slab we would expect to observe considering the 150 Ma long history of Farallon-JdF subduction. The slab extends to only 300 km depth beneath Oregon (Figures 2h and S7). The Gorda section of the slab is continuously imaged to greater depths around 600 km (Figure 2i). East of the Gorda slab, our model shows several fast features with amplitudes comparable to that of the Gorda slab (Figures 2i and S8, "F1" and "F2" in Figure 3). The shallow part of the fast feature immediately east of the Gorda slab and with a similar dip (Figure 2i, "F1" in Figure 3) was previously interpreted as lithospheric drip [*West et al.*, 2009]. The more horizontal fast anomaly further east (F2, Figures 2h, 2i, and 3f) has been previously imaged and interpreted as the Farallon plate foundering in the mid-mantle [*Sigloch et al.*, 2008]. Regionally, similar fast anomalies are not observed south of the southern boundary of the Gorda plate, i.e. south of ~38°N and the MTJ (Figures 2a and S2). We therefore interpret the fast bodies east of the presently subducting Gorda-JdF slab (anomalies F1 and F2) as possible fragments of the Farallon-JdF slab.

3.2. Yellowstone Anomaly

[6] The YSRP is underlain by an elongated northeast-southwest oriented low velocity anomaly (Figure 2a) that extends as deep as 300 km (Figures 2d–2g). The shallow anomaly is connected to an elongated low velocity body that extends continuously downward to a depth of 900 km (Figures S9 and S10). This observation contrasts with previous large-scale models [*Sigloch et al.*, 2008; *Burdick et al.*, 2009] for which no slow material is imaged in the transition zone. However, it is consistent with regional models in which the slow anomaly is continuously observed down to ~660 km where resolution is lost due to the limited aperture of the arrays [*Waite et al.*, 2006; *Yuan and Dueker*, 2005; *Smith et al.*, 2009]. The low-velocity anomaly dips to the northwest in the upper 400 km and to the southeast from 400 to 800 km depth (Figures 2f and 2g). The "S"-shape structure of the anomaly is similarly observed in both our P- and S-wave models (Figures 2d–2g).

4. Discussion

4.1. Juan de Fuca Slab

[7] The geometry of the Cascadia subduction zone, especially its north-south variation and the absence of a slab deeper than 300 km beneath Oregon, carries important implications for the tectonic setting of the Pacific Northwest. Beneath Oregon, the slab is too short to act as a mechanical barrier to upper-mantle flow and may allow the mantle underlying the JdF plate to flow eastward beneath the plate margin as the North American plate moves southwestward above it. This provides a possible explanation for the trench-

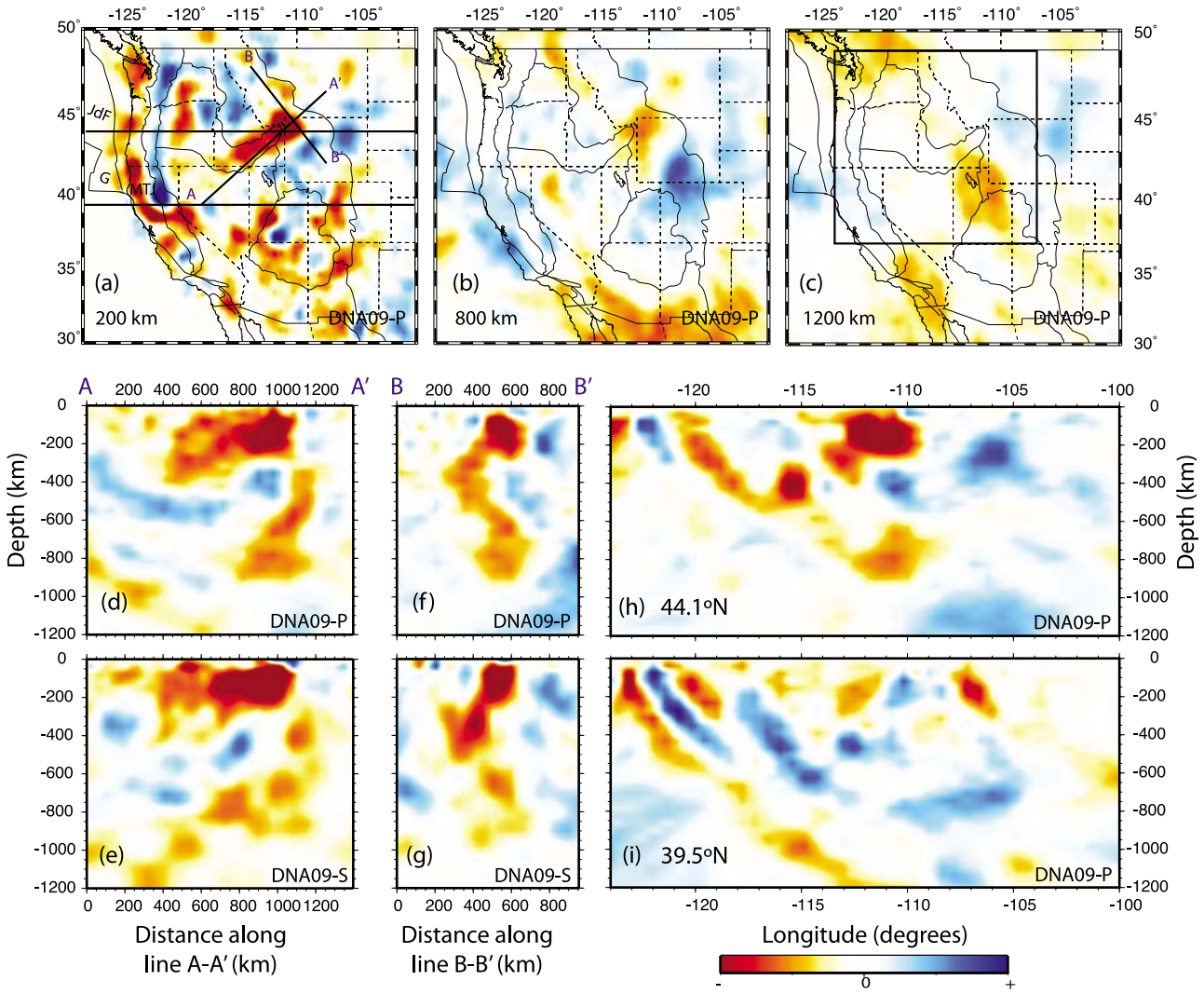

Figure 2. Map views and vertical cross sections showing the velocity structure of the Cascadia subduction zone and the Yellowstone anomaly. Constant depth slices at 200 km, 800 km and 1200 km extracted from our P-wave model. (a) Slow elongated anomaly beneath the YSRP and the along strike variation in amplitude of the north-south JdF slab anomaly. (b and c) Slow lower mantle beneath the Yellowstone Caldera as deep as the base of our model. (d and e) SW-NE cross-sections through our P- and S-wave models, respectively, along the YSRP (AA′, location shown in Figure 2a). These slices illustrate the deflection of the top of the Yellowstone anomaly by the southwestward moving North American plate. The amplitude of the slow anomaly increases to the northeast, where volcanism is younger. (f and g) NW-SE cross-sections though the Yellowstone Caldera along line BB′. They show the tilted low-velocity anomaly extending continuously from the surface to depth of 900 km. (h and i) Vertical slices at latitudes 39.5°N and 44.1°N, respectively. Figures 2h and 2i illustrate the fragmentation of the Gorda slab to the south and the shortness of the JdF Slab beneath Oregon. The color scale shown is −2 to +2% and −3 to +3% for our P- and S-wave models, respectively.

normal fast direction of anisotropy retrieved from SKS splitting analysis in central and northern Cascadia [*Long and Silver*, 2009, *Long et al.*, 2009; *Eakin et al.*, 2010]. The orientation of the fast direction in central and northern Cascadia differs from most other subduction zones where the fast direction is trench-parallel [*Long and Silver*, 2009]. The Gorda-Juan de Fuca slab is thought to be in trench rollback, and it has been suggested that the Gorda slab plays a significant role [*Humphreys and Coblentz*, 2007]. This is consistent with our model where the Gorda slab dives deeper into the mantle and exhibits a faster anomaly, potentially indicative of cooler and denser material. The retrograde motion of the Gorda-Juan de Fuca plate is also likely responsible for toroidal flow of the upper mantle around its southern edge as suggested by SKS splitting observations [*Zandt and Humphreys*, 2008]. Finally, the Cascadia subduction zone is also unusual due to the near-absence of deep seismicity (Figure 1). This has been previously associated with its young age and warm temperature [*Severinghaus and Atwater*, 1990]. The fragmentation of the slab may also play a role. There is no recorded seismicity >35 km depth beneath Oregon where the depth extent of the slab is only 300 km thereby reducing the slab pull force usually responsible for intermediate depth down-dip-tension earthquakes.

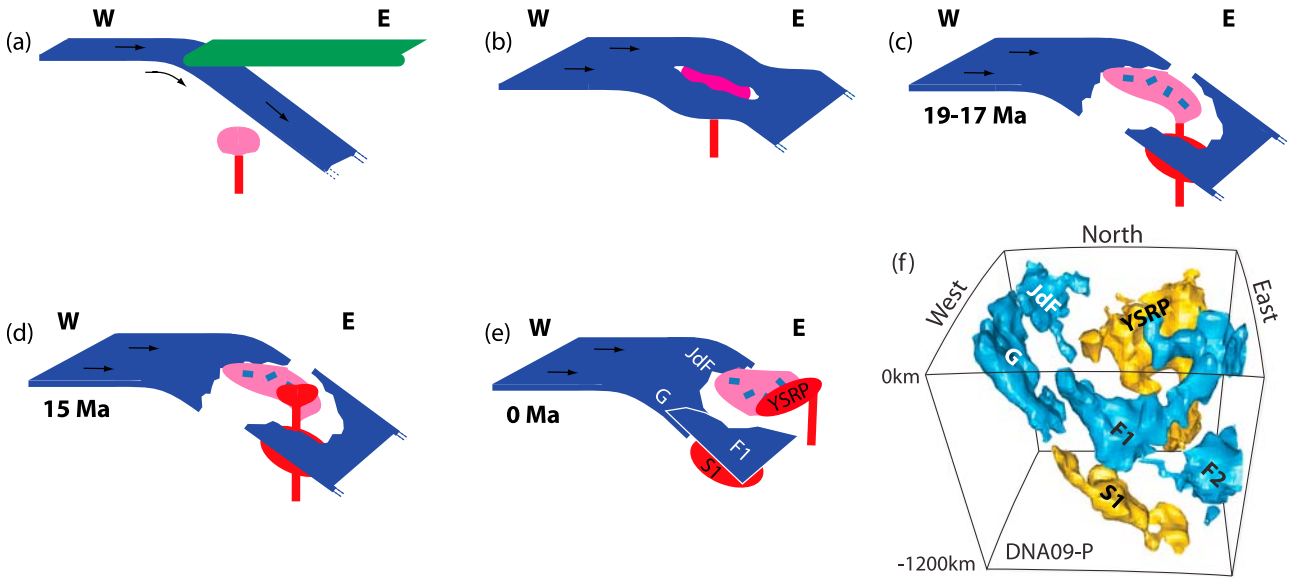

Figure 3. Illustrated time-history for the Pacific Northwest leading to today's mantle structure. (a) Any Yellowstone plume (pink plume head, red plume tail) would have to break through the subducting slab (blue) to reach the base of the continental lithosphere (green). (b) While the arrival of the buoyant plume likely precipitated break-up of the slab, pre-existing weaknesses and fractures may have facilitated the break. (c) The weakened slab eventually broke resulting in a reduction of slab pull and a decrease in the convergence rate at the trench at 19 Ma. Fragments of subducted oceanic crust (blue blocks) were assimilated by the plume head. The plume continued to the surface triggering the Columbia River Basalt outpouring. Some of the plume material may have remained trapped beneath remnants of the slab. (d) By ~15 Ma, the plume tail immerged to the south of the plume head and started propagating to the NE with respect to the North American plate. (e) As subduction continued, the fragment of the old slab (F1) and the currently subducting slab (G) began to overlap (as in Figure 2i). (f) Simplified 3D views (looking to the east) of our P-wave model. The depth of the box is 1200 km and the area plotted is that included in the box in Figure 2c. 3D isosurfaces that emphasize the structure of the JdF slab fragments and that of the Yellowstone plume are drawn at −0.3% and +0.45% (see also Figure S12).

There is some sub-crustal seismicity beneath Northern California and beneath Northern Washington where the slab is imaged deeper into the mantle (Figure 3).

4.2. Yellowstone Plume

[8] We interpret the low velocity anomaly beneath the YSRP as a mantle plume with a lower mantle origin. Our interpretation, based on geometrical observations of our P- and S-wave models, is also supported by the high He^3/He^4 isotopic ratio typical of the YSRP volcanism [*Graham et al.*, 2009], which is often interpreted as indicative of lower mantle source. The low-velocities are consistent with high temperatures and low-density. A hot plume with a large volume of low-density material, as observed in our models, accounts for the high heat flow, the broad topographic swell, the geoid high and the large free air gravity anomaly observed in the YSRP area [see *Smith et al.*, 2009, and references therein]. At 410 km depth the conduit is offset to the northwest of the Yellowstone Caldera and coincides with a region where the 410 km discontinuity deepens by 10 km [*Fee and Dueker*, 2004] as predicted when a high-temperature plume interacts with the transition zone. The geometry and structure of the elongated slow anomaly beneath the YSRP is consistent with the predictions of numerical models for the deflection of a plume head by the motion of an overlying lithospheric plate [*Lowry et al.*, 2000; *Steinberger et al.*, 2004]. It is elongated in the SW-NE direction parallel to the motion of the North American plate, the amplitude of the slow anomalies decrease to the southwest with increasing age of the calderas, and the plume conduit today coincides with active volcanism in the Yellowstone Caldera. This shallow, elongated part of the plume head exhibits a larger amplitude velocity anomaly than the conduit. The estimate we obtained for the Vp/Vs ratio from the comparison of our P-wave and S-wave models is also high for the shallow, elongated part of the anomaly (Figure S11). Both these observations are consistent with the presence of partial melt, which decreases preferentially S-wave velocities.

[9] The continuous body of the plume seems to bottom at 900 km. Below, we image another slow feature offset to the southwest of the Yellowstone Caldera (Figures 2c and S7, "S1" in Figure 3). A similar slow feature is also imaged in global tomographic models. This anomaly is offset from the plume conduit today (Figure 3) and sits beneath a region of the mantle that is dominated by fast features (Figure 2i and "F1", "F2" in Figure 3). Its origin is unclear. One possibility is that it is a remnant of the early plume that is now trapped beneath the string of high velocity slab fragments.

4.3. Plume Slab Interaction

[10] The existence of a whole-mantle plume and an active subduction zone within 1000 km of one another as imaged in our models makes the tectonic setting of the Pacific Northwest unique [*Davaille et al.*, 2005]. Also striking is the substantial fragmentation of the slab. The latitude where the

slab is absent coincides with that of the Yellowstone plume (Figure 3). Around 19 Ma there was a substantial change in the spreading rate at the Pacific-JdF ridge and also in the convergence rate of the Cascadia trench [*Wilson*, 1988]. This change could result from a reduction in slab pull. The change also shortly predates the massive magma outpouring of the Columbia River Basalts (CRB) and the onset of volcanism along the YSRP which have been interpreted as the manifestation of Yellowstone plume head emplacement [*Smith et al.*, 2009] around 17 Ma. We thus propose that the ascent of the Yellowstone plume, and its necessary encounter with the JdF slab, contributed to a rupture of the slab [*Xue and Allen*, 2007] (Figure 3) and the subsequent reduction of slab pull in the Cascadia trench. The composition of the CRB requires the presence of oceanic crust in the source [*Takahahshi et al.*, 1998], which supports the hypothesis that the Yellowstone plume interacted with the JdF slab and carried fragments of oceanic crust back up to the melting zone.

[11] How did the plume manage to pass through an oceanic slab? The proximity of the Pacific-JdF ridge to the Cascadia trench means that the slab was (and is) very young (~10 Ma at the trench) and therefore thin and warm. Erosion and fragmentation of the slab by the plume may have been facilitated and guided by preexisting weaknesses or tears in the slab. In the Oligocene-Miocene context of regional plate reorganization, the subducting slab may have been torn due to offshore fragmentation of the Pacific-JdF ridge when it approached the North American trench [*Severinghaus and Atwater*, 1990]. The Blanco Fracture zone (Figure 1) is located at the transition from very short slab (300 km) in central and northern Cascadia, to longer slab (600 km) in southern Cascadia. Earlier tearing of the slab may also have been caused by the accretion of the Siletzia terrane ~48 Ma and the induced trench jump at the end of the Laramide Orogeny (45 Ma) that occurred at the latitude of today's Oregon-Washington border [*Humphreys*, 2008], precisely where the slab is missing.

[12] Fragmentation of the slab presumably occurred just prior to the arrival of the plume at the surface, around 19–17 Ma. The trench-perpendicular subduction rate in southern Cascadia is 30 mm/yr, and has been relatively constant [*Wilson*, 1988] for the last 19 Ma. Slab subducted since the arrival of the plume at the surface would be expected to have reached ~500 km depth given the 60° dip, similar to the depth extent observed. The original obstruction to the plume by the slab, and the continuing presence of slab fragments in the mantle, mean that the plume's buoyancy-driven ascent path will deviate from vertical as it interacts with these obstructions. This plume-slab interaction may be responsible for the S-geometry of the plume depicted in Figures 2e and 2h.

[13] **Acknowledgments.** We thank USArray TA for data collection and the IRIS DMC for data distribution. This work was supported by the National Science Foundation and a UC-National Laboratory Research program grant.

References

Bunge, H.-P., and S. Grand (2000), Mesozoic plate-motion history below the northeast Pacific Ocean from seismic images of the subducted Farallon slab, *Nature*, *405*, 337–340, doi:10.1038/35012586.

Burdick, S., C. Li, V. Martynov, T. Cox, J. Eakins, T. Mulder, L. Astiz, F. L. Vernon, G. L. Pavlis, and R. D. van der Hilst (2009), Model update December 2008: Upper mantle heterogeneity beneath North America from travel time tomography with global and USArray transportable array data, *Seismol. Res. Lett.*, *80*(4), 638–645, doi:10.1785/gssrl.80.4.638.

Camp, V. E., and M. E. Ross (2004), Mantle dynamics and genesis of mafic magmatism in the intermontane Pacific Northwest, *J. Geophys. Res.*, *109*, B08204, doi:10.1029/2003JB002838.

Christiansen, R. L., G. R. Foulger, and J. R. Evans (2002), Upper-mantle origin of the Yellowstone hotspot, *Geol. Soc. Am. Bull.*, *114*, 1245–1256, doi:10.1130/0016-7606(2002)114<1245:UMOOTY>2.0.CO;2.

Davaille, A., E. Stutzmann, G. Silveira, J. Besse, and V. Courtillot (2005), Convective patterns under the Indo-Atlantic ≪box≫, *Earth Planet. Sci. Lett.*, *239*, 233–252, doi:10.1016/j.epsl.2005.07.024.

Dickinson, W. R. (1997), Tectonic implications of Cenozoic volcanism in coastal California, *Geol. Soc. Am. Bull.*, *109*, 936–954, doi:10.1130/0016-7606(1997)109<0936:OTIOCV>2.3.CO;2.

Eakin, C. M., et al. (2010), Seismic anisotropy beneath Cascadia and the Mendocino Triple Junction: Interaction of the subducting slab with mantle flow, *Earth Planet. Sci. Lett.*, doi:10.1016/j.epsl.2010.07.015, in press.

Fee, D., and K. Dueker (2004), Mantle transition zone topography and structure beneath the Yellowstone hotspot, *Geophys. Res. Lett.*, *31*, L18603, doi:10.1029/2004GL020636.

Graham, D. W., M. R. Reid, B. T. Jordan, A. L. Grunder, W. P. Leeman, and J. E. Lupton (2009), Mantle source provinces beneath the northwestern USA delimited by helium isotopes in young basalts, *J. Volcanol. Geotherm. Res.*, *188*, 128–140, doi:10.1016/j.jvolgeores.2008.12.004.

Humphreys, E. D. (2008), Cenozoic slab windows beneath the western United States, in *Ores and Orogenesis Circum-Pacific Tectonics, Geologic Evolution, and Ore Deposits*, edited by J. E. Spencer and S. R. Titley, *Ariz. Geol. Soc. Dig.*, *22*, 389–396.

Humphreys, E. D., and D. D. Coblentz (2007), North American dynamics and western U.S. tectonics, *Rev. Geophys.*, *45*, RG3001, doi:10.1029/2005RG000181.

Humphreys, E. D., K. G. Dueker, D. L. Schutt, and R. B. Smith (2000), Beneath Yellowstone: Evaluating plume and nonplume models using teleseismic images of the upper mantle, *GSA Today*, *10*(12), 1–7.

Long, M. D., and P. G. Silver (2009), Mantle flow in subduction systems: The subslab flow field and implications for mantle dynamics, *J. Geophys. Res.*, *114*, B10312, doi:10.1029/2008JB006200.

Long, M. D., H. Gao, A. Klaus, L. S. Wagner, M. J. Fouch, D. E. James, and E. D. Humphreys (2009), Shear wave splitting and the pattern of mantle flow beneath eastern Oregon, *Earth Planet. Sci. Lett.*, *288*, 359–369, doi:10.1016/j.epsl.2009.09.039.

Lowry, A. R., N. M. Ribe, and R. B. Smith (2000), Dynamic elevation of the Cordillera, western United States, *J. Geophys. Res.*, *105*(B10), 23,371–23,390, doi:10.1029/2000JB900182.

Pierce, K. L., and W. J. Morgan (1992), The track of the Yellowstone hotspot: Volcanism, faulting, and uplift, in *Regional Geology of Eastern Idaho and Western Wyoming*, edited by P. K. Link, M. A. Kuntz and L. B. Platt, *Geol. Soc. Am. Mem.*, *179*, 1–53.

Pierce, K. L., L. A. Morgan, and R. W. Saltus (2000), Yellowstone plume head: Postulated tectonic relations to the Vancouver slab, continental boundaries and climate, *U.S. Geol. Surv. Rep.*, *00-498*.

Roth, J. B., M. J. Fouch, D. E. James, and R. W. Carlson (2008), Three-dimensional seismic velocity structure of the northwestern United States, *Geophys. Res. Lett.*, *35*, L15304, doi:10.1029/2008GL034669.

Severinghaus, J., and T. Atwater (1990), Cenozoic geometry and thermal state of the subducting slabs beneath North America, in *Basin and Range Extensional Tectonics Near the Latitude of Las Vegas, Nevada*, edited by B. P. Wernicke, *Geol. Soc. Am. Mem.*, *176*, 1–22.

Sigloch, K., N. McQuarrie, and G. Nolet (2008), Two-stage subduction history under North America inferred from multiple-frequency tomography, *Nat. Geosci.*, *1*, 458–462, doi:10.1038/ngeo231.

Smith, R. B., M. Jordan, B. Steinberger, C. M. Puskas, J. Farrell, G. P. Waite, S. Husen, W.-L. Chang, and R. O'Connell (2009), Geodynamics of the Yellowstone hotspot and mantle plume: Seismic and GPS imaging, kinematics, and mantle flow, *J. Volcanol. Geotherm. Res.*, *188*, 26–56, doi:10.1016/j.jvolgeores.2009.08.020.

Steinberger, B., R. Sutherland, and R. J. O'Connell (2004), Prediction of Emperor-Hawaii seamount locations from a revised model of global plate motion and mantle flow, *Nature*, *430*, 167–173, doi:10.1038/nature02660.

Takahahshi, E., K. Nakajima, and T. L. Wright (1998), Origin of the Columbia River basalts: Melting model of a heterogeneous mantle plume head, *Earth Planet. Sci. Lett.*, *162*, 63–80, doi:10.1016/S0012-821X(98)00157-5.

Waite, G. P., R. B. Smith, and R. M. Allen (2006), VP and VS structure of the Yellowstone hot spot from teleseismic tomography: Evidence for an

upper mantle plume, *J. Geophys. Res.*, *111*, B04303, doi:10.1029/2005JB003867.

West, J. D., M. J. Fouch, J. B. Roth, and L. T. Elkins-Tanton (2009), Vertical mantle flow associated with a lithospheric drip beneath the Great Basin, *Nat. Geosci.*, *2*, 439–444, doi:10.1038/ngeo526.

Wilson, D. S. (1988), Tectonic history of the Juan de Fuca Ridge over the last 40 million years, *J. Geophys. Res.*, *93*(B10), 11,863–11,876, doi:10.1029/JB093iB10p11863.

Xue, M., and R. M. Allen (2007), The fate of the Juan de Fuca plate: Implications for a Yellowstone plume head, *Earth Planet. Sci. Lett.*, *264*, 266–276, doi:10.1016/j.epsl.2007.09.047.

Yuan, H., and K. Dueker (2005), Teleseismic *P*-wave tomogram of the Yellowstone plume, *Geophys. Res. Lett.*, *32*, L07304, doi:10.1029/2004GL022056.

Zandt, G., and E. Humphreys (2008), Toroidal mantle flow through the western U.S. slab window, *Geology*, *36*, 295–298, doi:10.1130/G24611A.1.

R. M. Allen and M. Obrebski, Department of Earth and Planetary Science, University of California, 307 McCone Hall, Berkeley, CA 94705, USA. (obrebski@berkeley.edu)

S.-H. Hung, Department of Geosciences, National Taiwan University, No. 1, Sec. 4, Roosevelt Rd., Taipei 10617, Taiwan.

M. Xue, School of Ocean and Earth Science, Tongji University, 1239 Siping Rd., Shanghai 200092, China.

Auxiliary material for Geophysical Research Letters Paper 2010GL043489

Slab-Plume Interaction beneath the Pacific Northwest

Mathias Obrebski, **Richard M Allen**, University of California, Berkeley, USA
Mei Xue, Tongji University, China
Shu-Huei Hung, National Taiwan University, Taiwan

This file contains three self-contained sections:

1. Data and method
2. Comparison with previous tomographic models
3. Supplementary figures

Data and Method

In this paper, we compile a seismic waveform dataset consisting of teleseismic body-waves, both direct and core phases, recorded at seismic stations across the western United States. We focus on the western US as Earthscope USArray, the regional seismic networks and temporary seismic deployments together provide an array of more than 1000 seismometers with an unprecedented density and spatial extent (Fig A1).

Seismic data for this study was provided by the following networks: the Earthscope Transportable Array, two Earthscope Flexible Array deployments (FACES and Mendocino), Global Seismograph Network (IRIS/IDA and IRIS/USGS), Canadian National Seismograph Network (CNSN), GEOSCOPE (GEO), United States National Seismic Network (USNSN), ANZA Regional Network (ANZA), Berkeley Digital Seismograph Network (BDSN), Cascade Chain Volcano Monitoring Network (CC), Montana Regional Seismic Network (MRSN), Northern California Seismic Network (NCSN), Western Great Basin/Eastern Sierra Nevada Network (WGB/ESN), Southern California Seismic Network, University of Oregon Regional Network (UO), University of Utah Regional Network (UURN), Pacific Northwest Regional Seismic Network (PNSN), Yellowstone Wyoming Seismic Network (YWSN) and Wallowa.

Our dataset contains high quality body-wave compressional- and shear- arrivals recorded from January 2006 to July 2009. Special attention was paid to select only the highest quality data. Our initial dataset consisted of events with epicentral distance greater than 30 degrees and magnitude greater or equal to 5.5. After visual inspection, half of these events were discarded. Arrivals were picked manually as part of the waveform-by-waveform quality control and to provide a marker for the cross-correlation that followed. The resulting dataset consists of relative traveltime delays [VanDecar and Crosson, 1990]. Owing to the broad frequency content of the compressional waves, cross-correlograms were calculated in four frequency bands (0.02-0.1Hz, 0.1-0.4Hz, 0.4-0.8Hz, 0.8-2.0Hz). The shear waves have lower frequency content and only cross-correlograms in the 0.02-0.1Hz frequency band where found to have sufficiently high signal-to-noise ratio. Note that the frequency band used to obtain our S-velocity model corresponds to the lowest frequency band used to obtain our P-velocity model. Only arrivals that produce a mean correlation coefficient larger or equal to 0.9 are used in the inversion, reducing the total number of data by another ~50%. Our final compressional-arrival dataset is consists of 30,670 traveltime observations of direct P from 127 earthquakes. The shear-arrival dataset includes 58,670 travel-time measurements, 34,850 S-wave observations from 142 events and 3,900 SKS observations from 24 events.

In this study we combine this regional dataset with a tomographic technique utilizing finite frequency sensitivity kernels. The banana-doughnut-shaped kernels account for the frequency- and depth-dependent width of the region to which teleseismic body-waves are sensitive and account for wave-front healing effects. Our tomographic method uses paraxial kernel theory to calculate the

forward scattering sensitivity kernels for teleseismic arrival times [Dahlen et al., 2000; Hung et al., 2000; Hung et al., 2004]. Sensitivity kernels are calculated for each frequency band used to calculate the cross-correlograms obtained previously from compressional and shear arrivals. The model domain is a spherical cap centered at 39.5N 112.5W. The domain extends from 127W to 98W and 25N to 54N, and from the surface to a depth of 2500 km. There are 65 nodes in both horizontal and in the vertical directions. The model box is larger than the region in which we expect to have good resolution. By using relative arrival time measurements we assume that the sensitivities of all arrivals for a given earthquake are the same outside the model box. Using a large model box causes any anomalies outside the model region to be accommodated in the unresolved outer region of the model space preventing pollution of the primary target region beneath the seismic network.

Station corrections are included in the inversion to absorb traveltime delays common to each station, i.e. directly beneath the station. The inclusion of these additional parameters prevents what can be large crustal traveltime delays bleeding into mantle structure, but also means that the upper ~100 km of the velocity models do not represent true Earth structure [Allen et al., 2002]. Event corrections are also included to account for any baseline difference between events [VanDecar and Crosson, 1990]. The finiteness of the sensitivity kernels means there is no need for smoothing. Our inversion does require damping and uses LSQR to iterate to a final model. Trade-off curves between model norm and residual misfit were used to select the appropriate damping. The P and S models presented here have variance reductions of 79% and 71% respectively. Maps of the crustal corrections (Fig A1) show similar structure to other lithospheric models for North America [Bensen et al., 2008; Pollitz, 2008; Yang et al., 2008].

We refer to the models presented here as DNA09-P for the compressional velocity and DNA09-S for the shear velocity. The structure imaged in DNA09-P and -S are highly consistent between each other despite the difference in the wavelengths of the signals used (Fig A2). DNA09-P is a relatively short-wavelength model having a typical sensitivity kernel width of 80 km at 600km depth while DNA09-S is derived from longer wavelength seismic arrivals with typical kernel widths of 270 km at 600 km depth.

Checkerboard resolution tests with alternating high- and low-velocity cubes show good recovery beneath the seismic array to a depth of 1200km (Figs A3-A6), we therefore only interpret structures to 1200km depth. We also test the ability of the dataset to resolve specific geometries as guided by our interpretation. These include test of the surprisingly short slab beneath Oregon (Fig A7), the overlapping slabs beneath northern California (Fig A8), the continuous plume beneath the YSRP (Fig A9) and its sinuous shape (Fig A10).

References

Allen, R.M., G. Nolet, W. J. Morgan, K. Vogfjord, B. H. Bergsson, P. Erlendsson, G. R. Foulger, S. Jakobsdottir, B. R. Julian, M. Pritchard, S. Ragnarsson, and R. Stefansson (2002), Imaging the mantle beneath Iceland using integrated seismological techniques, J. Geophys. Res., 107(B12), 2325, doi: 10.1019/2001JB000595.

Bensen, G.D., M. H. Ritzwoller and N. M. Shapiro (2008), Broad-band ambient noise surface wave tomography across the United Stated, J. Geophys. Res., 113, B05306, doi:10.1029/2007JB005248.

Dahlen, F. A., S. H. Hung, and G. Nolet (2000), Frechet kernels for finite-frequency traveltimes, I. Theory, Geophys. J. Int., 141, 157-174.

Hung, S.H., F. A. Dahlen, and G. Nolet (2000), Frechet kernels for finite-frequency traveltimes, II. Examples, Geophys. J. Int., 141, 175-203.

Hung, S. H., Y. Shen, and L. Y. Chiao (2004), Imaging seismic velocity structure beneath the Iceland hot spot: A finite frequency approach, J. Geophys. Res., 109, B08305.

Pollitz, F. F. (2008), Observations and interpretation of fundamental mode Rayleigh wavefields recorded by the Transportable Array (USArray), J. Geophys. Res., 113, B10311, doi:10.1029/2007JB005556.

VanDecar, J. C., and R.S. Crosson (1990), Determination of teleseismic relative phase arrival times using multi-channel cross-correlation and least squares, Bull. Seism. Soc. Am., 80, 150-169.

Yang, Y., M. H. Ritzwoller, F. C. Lin, M. P. Moschetti, and N. M. Shapiro (2008), The structure of the crust and uppermost mantle beneath the western US revealed by ambient noise and earthquake tomography, J. Geophys. Res., 113, B12310, doi:10.1029/2008JB005833.

Comparison with previous tomographic models

Here we compare our P- and S-wave based tomographic models with those previously published by Roth et al [2008], Sigloch et al. [2008] and Burdick et al. [2009]. These three models also use data including but not limited to the Earthscope USArray deployment and are P-wave models. We also compare our model with more regional studies around Yellowstone and published by Waite et al. [2006], Yuan and Dueker [2005] and Smith et al. [2009]. We only discuss the area between roughly 35 and 49 degrees north, and 125 and 105 degrees east, which is part of the region where the resolution of our model is good, and where the tectonic features discussed in the main text of the article are located, chiefly the Juan de Fuca-Gorda slab and the Yellowstone anomaly.

The structure of the slab is imaged in a very similar way in most USArray-based tomographic models. In particular, it consistently exhibits a weak signature beneath Oregon (Roth et al., 2008, Figure 2; Sigloch et al., 2008, Figure 2; Burdick et al., 2009, Figure 5; this study Figure 2a, 2h, 3f). Roth et al. [2008] suggest the weak signature is an artefact produced by the slow velocities located in the wedge above the slab beneath Oregon. Synthetic tests presented in Burdick et al. [2009] and in this study (Figure A8) rather suggest that the absence of slab is a well-resolved feature. Beneath northern California, the slab is well imaged as deep as the transition zone in most models (Roth et al., 2008, Figure 2; Burdick et al., 2009, Figure 5; this study Figures 2i and 3f). Finally, beneath Washington, the shape of the slab is not straightforward to visualize as its signature merges with a fast anomaly located beneath eastern Washington, north-eastern Oregon and Idaho (Roth et al 2008, Figure 2, feature labelled "IB"; Burdick et al., 2009, Figure 6, cross-section AA'; this study Figure 2a).

East from the westernmost fast anomaly located beneath the Cascadia trench and that we interpret as the currently subducting Gorda slab, several other fast features are present in our model, in agreement with previous studies. The anomaly that we labelled F1 in Figure 3 is also seen in Roth et al. [2008] (Figure 2F, feature labelled "SSA"), Burdick et al. [2009] (Figure 5: constant depth map views at 400, 500 and 600km; Figure 6: cross-section B-B'), and Sigloch et al. [2008] (Figure 1, cross-section at 42 degrees north, feature labelled "S1"). The shallower part of F1 has been interpreted as lithospheric drip by West et al [2009]. In the model of Sigloch et al. [2008], S1 ("F1" in our study) is not clearly connected with the shallower 400km of the currently subducting slab that has a rather weak signal in their 42°N cross-section. They interpret S1 ("F1" in our study) as the subducting slab. Farther east, we observe in our model a deeper fast anomaly that we labelled F2 in Figure 3. This feature is also well observed in the model of Sigloch et al. [2008] ("S2", Figure 1, cross-section at 42°N). They interpret this last feature as the continuation of the subducting slab. Note that the Sigloch model uses data from stations located all over the USA, so it benefits from good resolution farther east than any other model mentioned here and also from a larger aperture, i.e. deeper resolution. This means that "S2" ("F2" in this study) is well resolved in the study of Sigloch et al. [2008].

The horizontally elongated shallow part of the Yellowstone anomaly appears consistently in all models in the upper 250km beneath the Yellowstone Snake River Plain. In contrast, the deeper part of the Yellowstone anomaly shows variations from one model to another. In Sigloch et al. [2008], it appears only from 500-1000km (Figure 1B). Sigloch et al. [2008] interpret this deep low anomaly as the former source of the Columbia River flood basalts 17Myr ago. The vertical low-velocity anomaly that we interpret as the Yellowstone plume is at the edge of the model presented in Roth et al. [2008]. In the model of Burdick et al. [2009], the Yellowstone anomaly does not appear in the

transition zone (Figure 6, cross-section DD'). Studies prior to USArray using regional datasets do show that the Yellowstone anomaly extends continuously from the surface to the bottom on the transition zone in Waite et al. [2006], Yuan and Dueker [2005] and Smith et al. [2009]. Deeper, these regional models loose resolution due to there limited aperture.

References

Burdick, S., C. Li, V. Martynov, T. Cox, J. Eakins, T. Mulder, L. Astiz, F. L.Vernon, G. L. Pavlis, and R. D. van der Hilst (2009), Model Update December 2008: Upper mantle heterogeneity beneath north America from travel time tomography with global and USArray transportable array data, Seism. Res. Lett., 80(4), 638-645.Camp, V. E. and M. E. Ross (2004), Mantle dynamics and genesis of mafic magmatism in the intermontane Pacific Northwest, J. Geophys. Res., 109, B08204, doi:10.1029/2003JB002838.

Roth, J. B., M. J. Fouch, D. E. James, and R. W. Carlson (2008), Three-dimensional seismic velocity structure of the northwestern United States, Geophys. Res. Lett., 35, L15304, doi:10.1029/2008GL034669.

Sigloch, K., N. McQuarrie, and G. Nolet (2008), Two-stage subduction history under North America inferred from multiple-frequency tomography, Nature Geoscience, 1, 458-462.

Waite, G. P., R. B. Smith, and R. L. Allen (2006,) VP and VS structure of the Yellowstone hot spot from teleseismic tomography: Evidence for an upper mantle plume, J. Geophys. Res., 111, B04303, doi:10.1029/2005JB003867.

West, J. D., M. J. Fouch, J. B. Roth, and L. T. Elkins-Tanton (2009), Vertical mantle flow associated with a lithospheric drip beneath the Great Basin, Nature Geoscience, 2, 439-444.

Yuan, H. Y. and K. Dueker (2005), Teleseismic P-wave tomogram of the Yellowstone plume, Geophys. Res. Lett., 32.

Supplementary Figures

Fig A1. Maps of event and station corrections determined simultaneously in the inversions for DNA09-P and -S. These corrections account for traveltime delays common to all arrivals for an event, or all arrivals at a station. The station corrections absorb delays from the shallow structure beneath each station. The lithospheric signal includes reduced delays (higher velocities and/or thinner crust) beneath the Colorado Plateau, larger delays (low velocities and/or thicker crust) beneath the Basin and Range and very low velocities beneath the Yellowstone Caldera. Reduced delays are also found along the Cascadia Range and extending south into the Sierra, increased delays in the Central Basin of California. Comparison of the station corrections with other lithospheric models of the western US shows broad agreement as would be expected [Bensen et al., 2008; Pollitz, 2008; Yang et al., 2008].

Fig A2. Comparison between the DNA09-P and the DNA09-S models at 200km, 400km 600km and 800km. These map views show how the mantle is dominantly slow south from the Gorda slab and the Mendocino Triple Junction. To the north, the mantle contains a large amount of fast material that surrounds the Yellowstone anomaly.

Fig A3. Checkerboard resolution tests for DNA09-P with alternating high- and low-velocity cubes. The cubes are 250x250x250 km and the input (synthetic) velocities anomalies were +-2%. The synthetic velocity anomalies were used to calculate synthetic traveltimes to which random noise was added. For each traveltime delay the applied noise was derived by selecting randomly from a Gaussian distribution with a standard deviation equal to 15% of the traveltime delay. Vertical slices through the input and recovered velocity structures are shown. Above 1000km the resolution is very good with the exception of the shallow southwest corner beneath the Pacific due to the absence of stations. The resolution degrades a little in some of the deeper portions of the model. All velocity structure discussed in this paper and all images come from within this region of good resolution.

Fig A4. Same as Fig A3, except that horizontal slices through the input and recovered velocity structures are shown.

Fig A5. Checkerboard resolution tests for DNA09-S. The resolution tests are very similar to those shown in Figs A3 and A4 except that the cubes are 300x300x300km and the input velocity anomalies were +-4%.

Fig A6. Same as Fig A5, except that horizontal slices through the input and recovered velocity structures are shown.

Fig A7. Resolution tests with two slab-like features. The DNA09-P model is shown (a) along with the input synthetic velocity structures (b and d) to be tested and the output (c and e) velocity model obtained by inverting synthetic traveltime data derived from the input velocity models with noise applied in the same way as Fig A3. (a) is a vertical slice at latitude 39.5N where two slab-like anomalies are seen (Fig. 2i). The input synthetic velocity model (b) has a similar structure with two parallel dipping features with a +2% compressional velocity anomaly. The test shows these features are well recovered with our data coverage (c). In a similar vein, (d) and (e) show that the low velocity observed from 900km to 1200km is well resolved and does not result from smearing.

Fig A8. Resolution tests with a high-velocity slab-like feature overlaid by a low velocity elongated anomaly. The DNA09-P model is shown (a) along with the input synthetic velocity structures (b and d) to be tested and the output (c and e) velocity model obtained by inverting synthetic traveltime data derived from the input velocity models with noise applied in the same way as Fig A3 for the slices are all at a latitude of 44.1N as shown in Fig. 2h. This tests show that the structure of the slab is well resolved and that the absence of a deep slab is not an artifact induced by the presence of low velocity material immediately east and above the slab.

Fig A9. Resolution test investigating the continuity of the plume-like anomaly. Vertical slices are shown along the YSRP (a, c and e), and perpendicular to it through the Yellowstone Caldera (b, d and f). The input model (c and d) and the recovered structure (e and f) are shown. The input model consists of a sequence of three separate -3% compressional velocity anomalies placed beneath the Yellowstone Caldera. This test demonstrates that the continuous deep-seated mantle anomaly observed in DNA09-P is not the result of smearing distinct low-velocity anomalies. The location of those slices is the same as in Fig. 2d to 2g.

Fig A10. Same as Fig A9 but using a continuous, straight cylinder as an input structure. This test shows that the S-shape of the plume conduit is not due to distortion of a vertical conduit by the available seismic dataset and also that the anomaly does not smear to greater depth.

Fig A11. Vertical slices along and across the Yellowstone anomaly in DNA09-P, DNA09-S and an estimate of the Vp/Vs ratio derived from the DNA09-P and -S models. The d(Vp/Vs)/(Vp/Vs) anomaly on the Poisson Ratio is the difference between dVp/Vp and dVs/Vs, the anomalies on Vp and Vs, respectively:

$$d(Vp/Vp)/(Vs/Vs) = (VsdVp-VpdVs)/Vs/Vs * (Vs/Vp) = dVp/Vp - dVs/Vs$$

The location of the slices is the same as in Fig. 2d to 2g and A9. The figure shows that the elongated slow velocity beneath the YSRP has high Vp/Vs ratio, which is suggestive of partial melting.

Fig A12. 3D views of DNA09-P. The depth of the box is 1200km and the area plotted is that included in the box in Fig. 2c. (a) shows all 3D isosurfaces drawn at -0.3% and +0.45%. (b) and (c) are simplified views that emphasize the structure of the JdF slab fragments and that of the Yellowstone plume. (b) is a view to the north looking in the plane of the subducting JdF and Gorda (G) slabs. (c) is a view to the east illustrating the gap in the slab and the low velocity anomalies east of the gap. In (b) and (c) the southern edge of the JdF-Gorda slab at the Mendocino Triple Junction is clearly observed. The bottom edge of the slab is at variable depths and even absent beneath Oregon as shown in Fig. 2h. We interpret anomalies F1 and F2 as possible slab fragments because these fast features have

amplitude similar with the currently subducting Juan de Fuca-Gorda slab, they are aligned with it and they do not appear south from the southern tip of the Gorda slab, where the tectonic setting changes from subduction beneath the Cascades to strike-slip motion along the San Andreas Fault. The high velocity body in the upper 400 km of the mantle that strikes NE and is located beyond F1 may be part of the cratonic root. (d) and (e) are views to the northwest and southwest, respectively, that emphasize the structure of the Yellowstone anomaly.

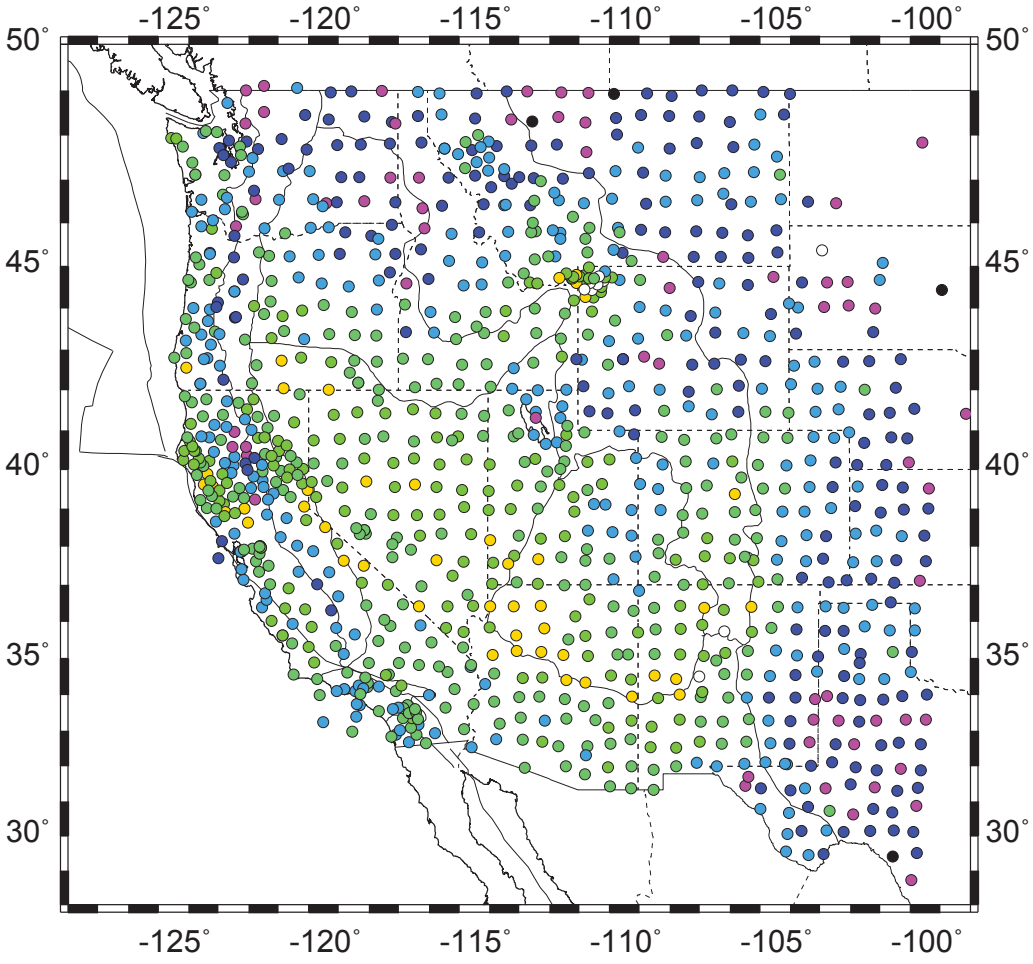

DNA09-P

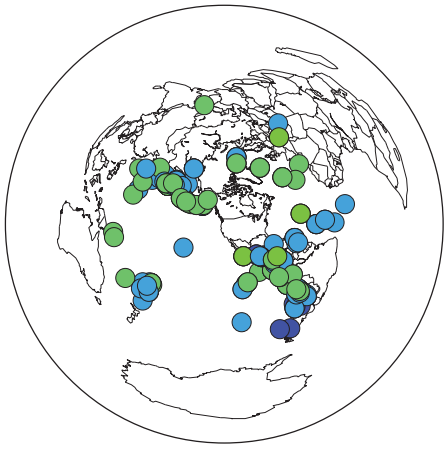

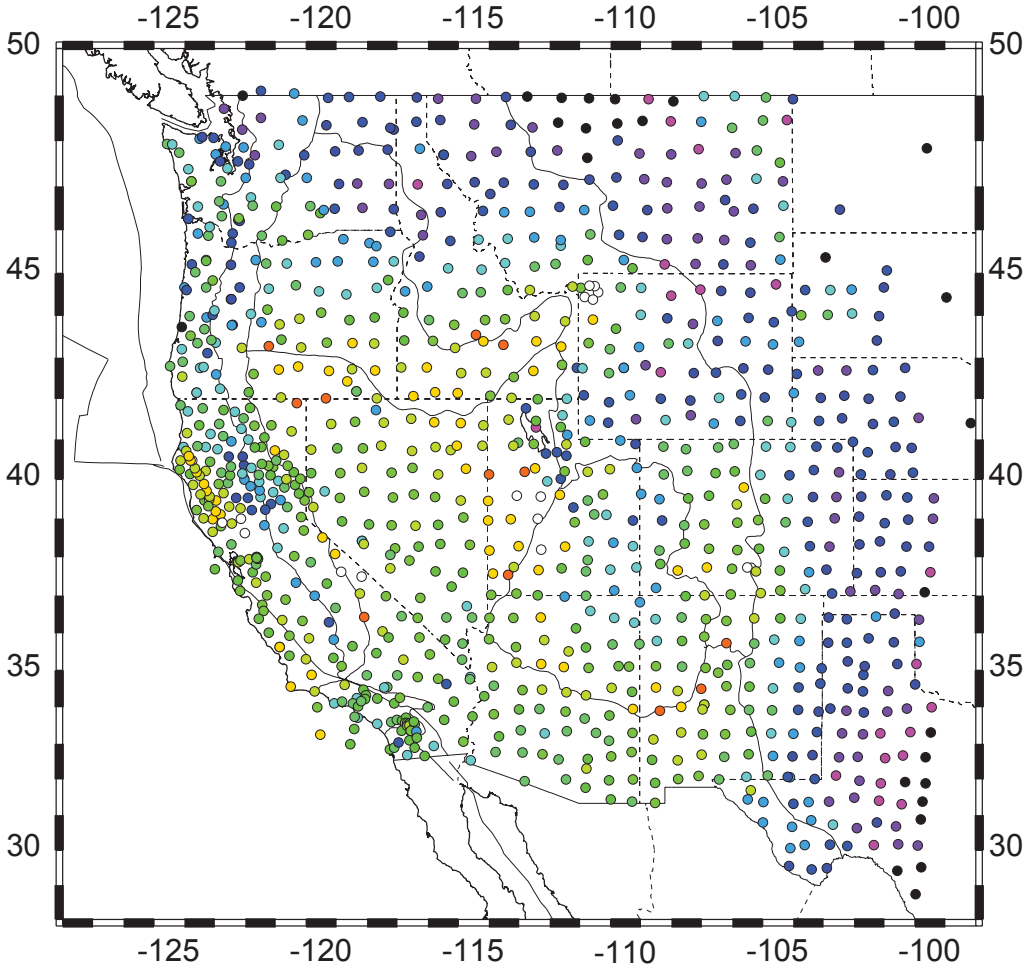

DNA09-S

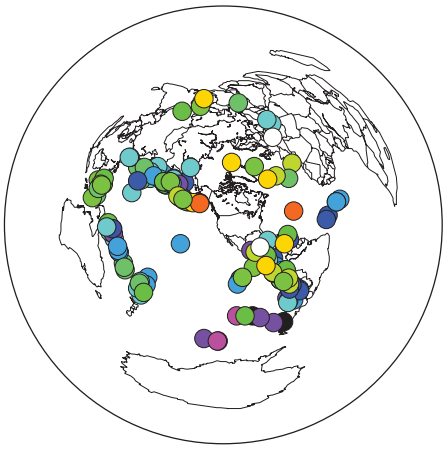

Fig. A1

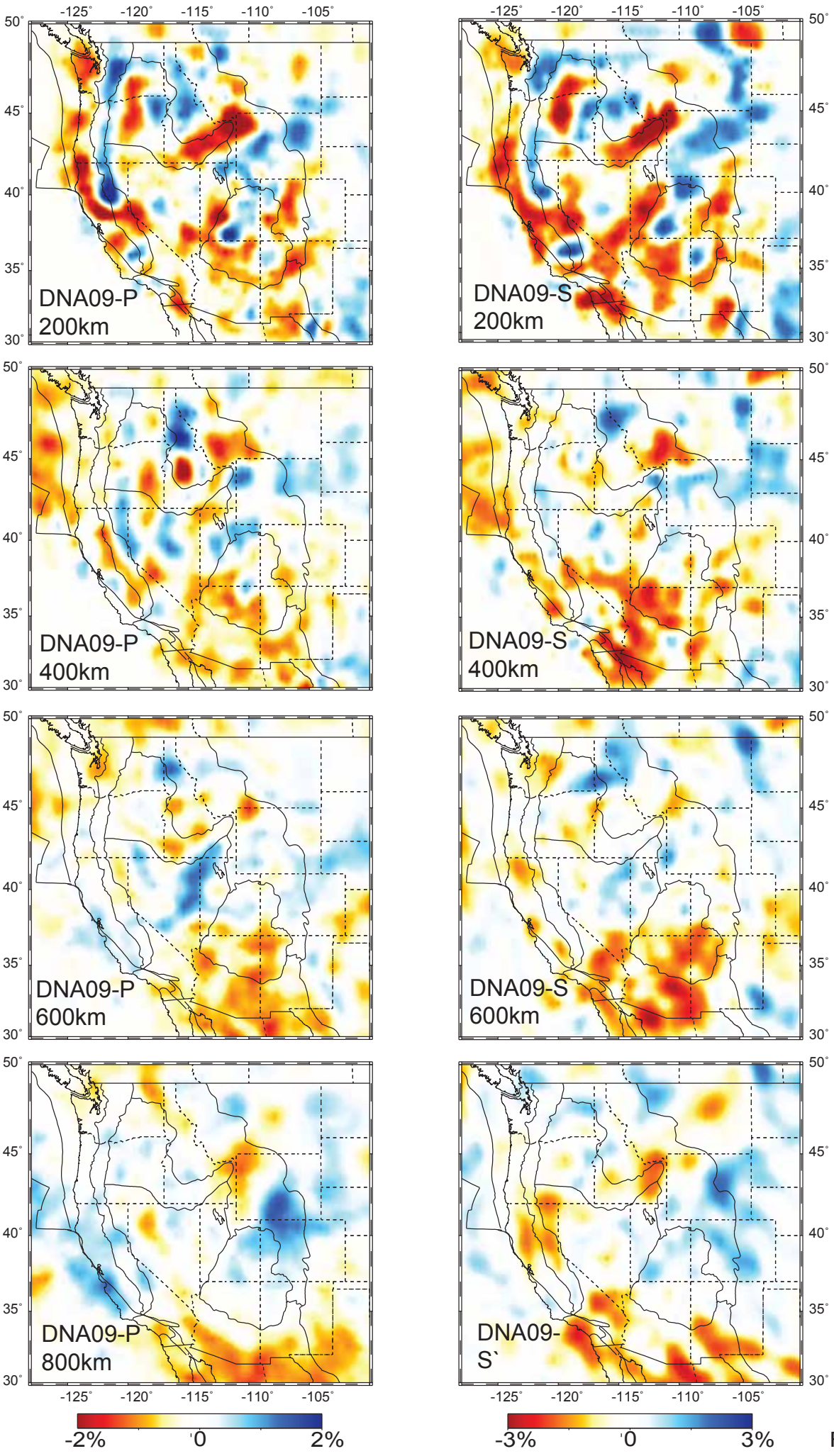
DNA09-P
200km
DNA09-S
200km
DNA09-P
400km
DNA09-S
400km
DNA09-P
600km
DNA09-S
600km
DNA09-P
800km
DNA09-
S`
-125˚
-120˚
-115˚
-110˚
-105˚
50˚
45˚
40˚
35˚
30˚
-2%
0
2%
-3%
0
3%

Fig. A2

DNA09-P

Input
(250x250x250km)

Output

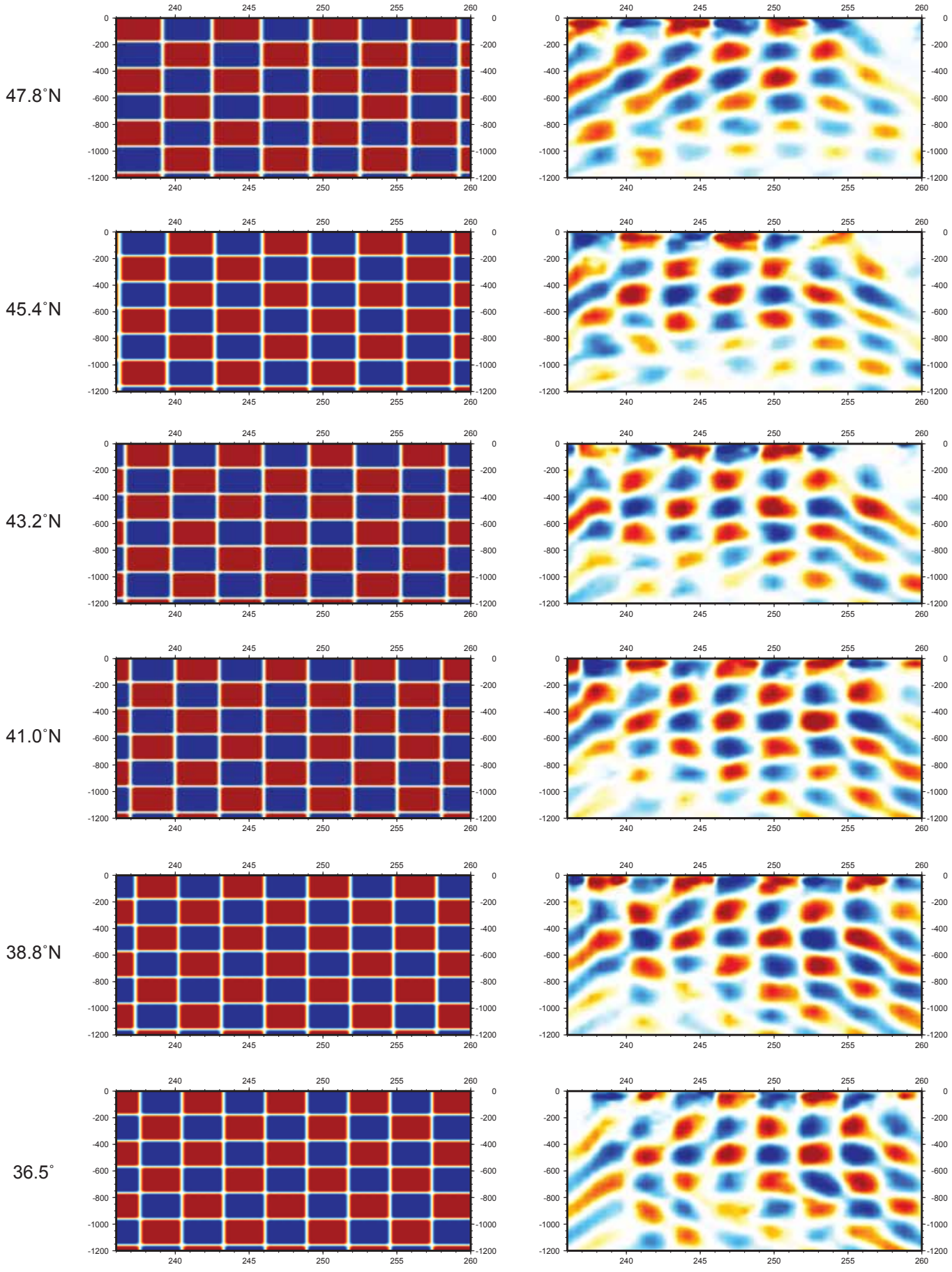

-1.5% 0 +1.5%

Fig. A3

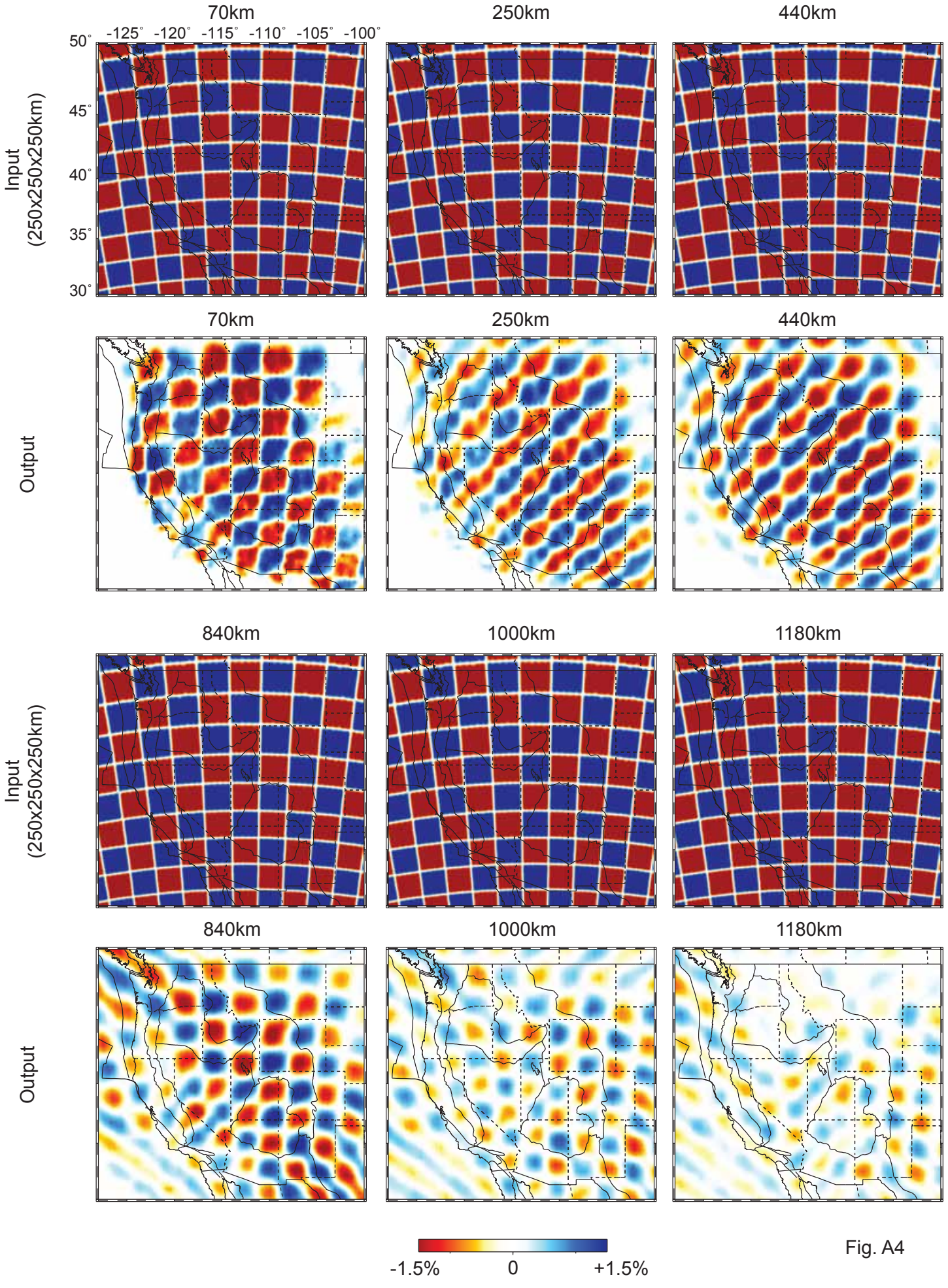
DNA09-P
70km
250km
440km
-125˚ -120˚ -115˚ -110˚ -105˚ -100˚
50˚
45˚
40˚
35˚
30˚
Input (250x250x250km)
Output
70km
250km
440km
840km
1000km
1180km
Input (250x250x250km)
Output
840km
1000km
1180km
-1.5%
0
+1.5%

Fig. A4

DNA09-S

Input
(300x300x300km)

Output

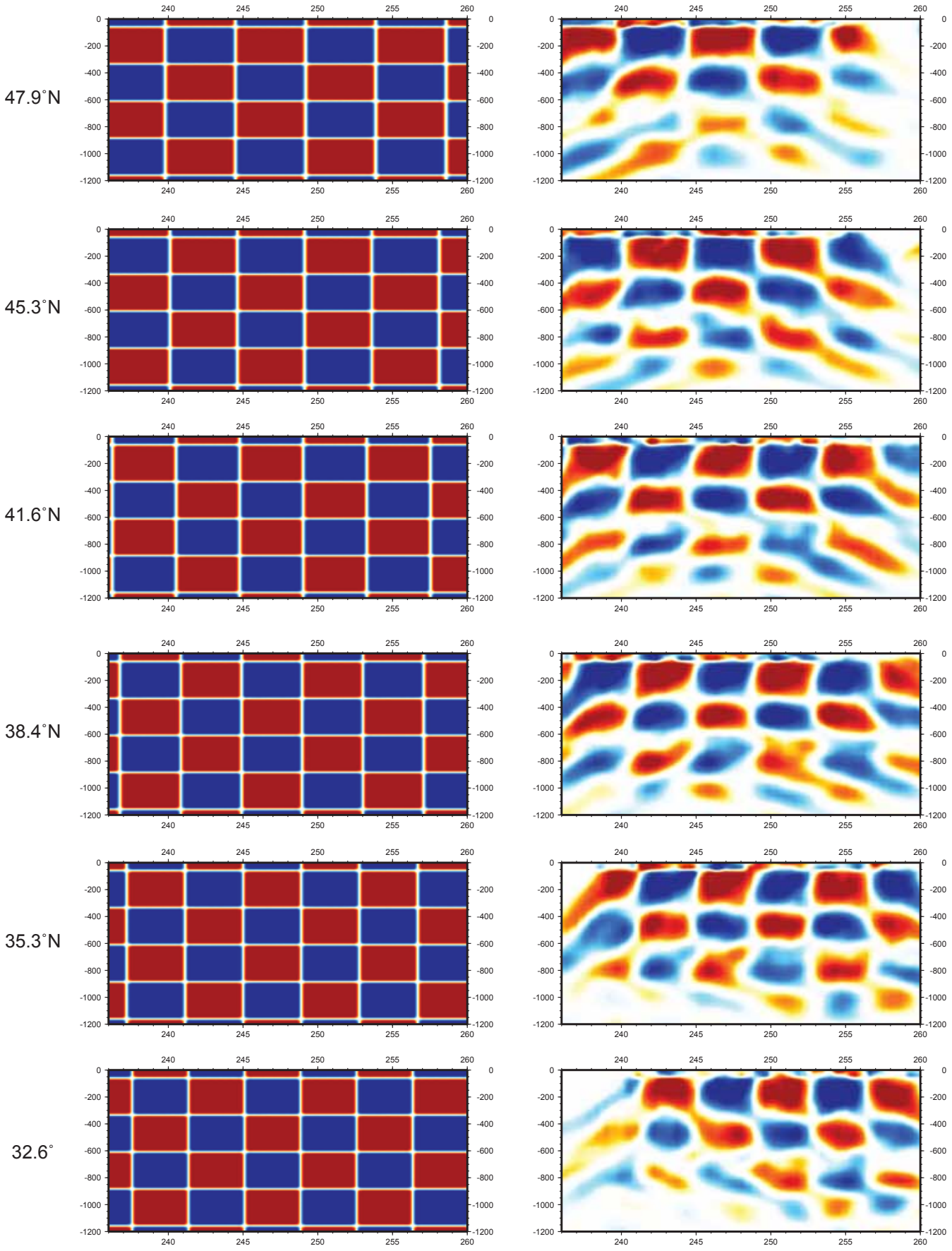

-3.0% 0 +3.0%

Fig. A5

DNA09-S

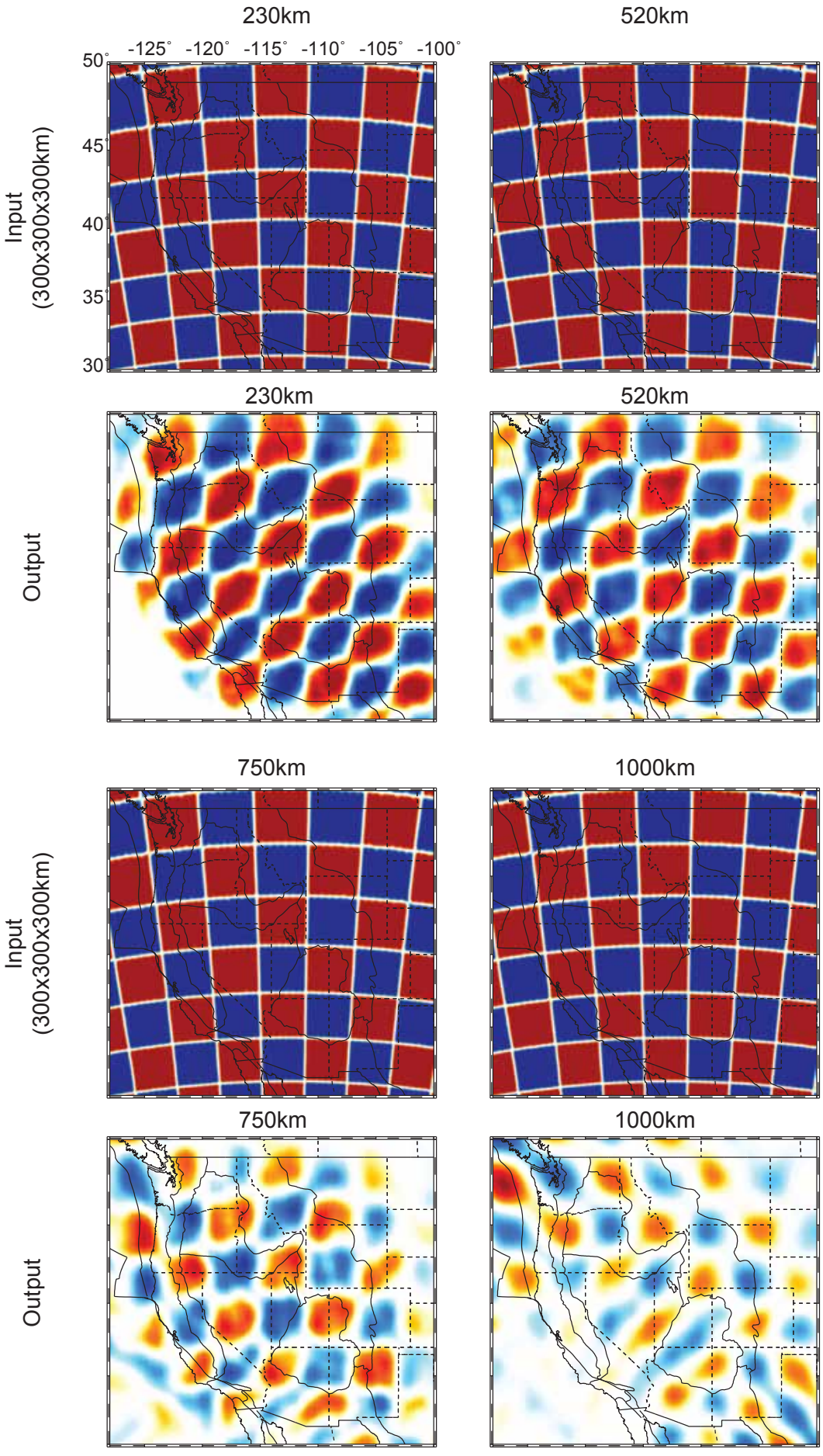

Fig. A6

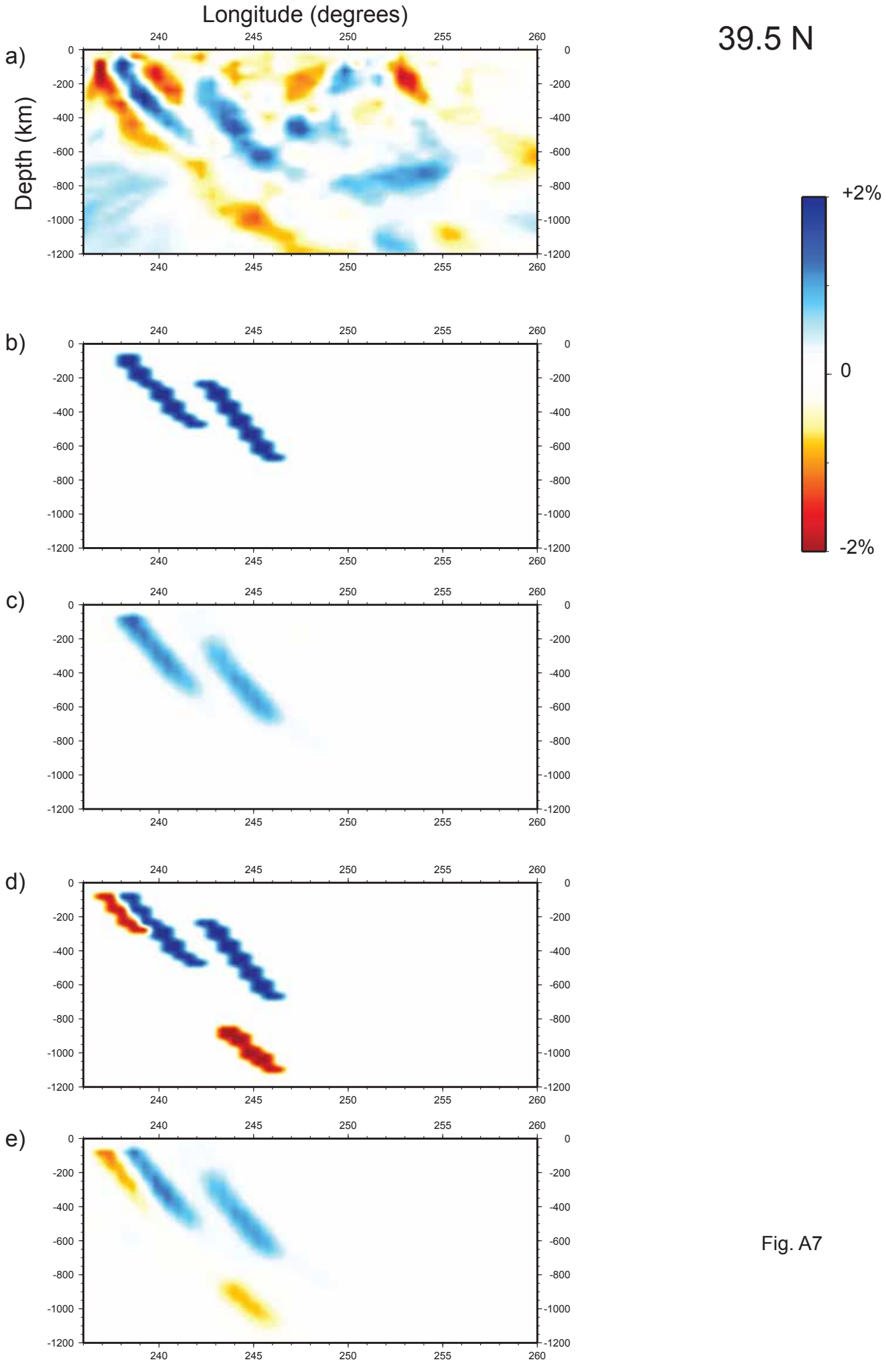
Longitude (degrees)
39.5 N
Depth (km)
a)
b)
c)
d)
e)
240
245
250
255
260
0
-200
-400
-600
-800
-1000
-1200
+2%
0
-2%

Fig. A7

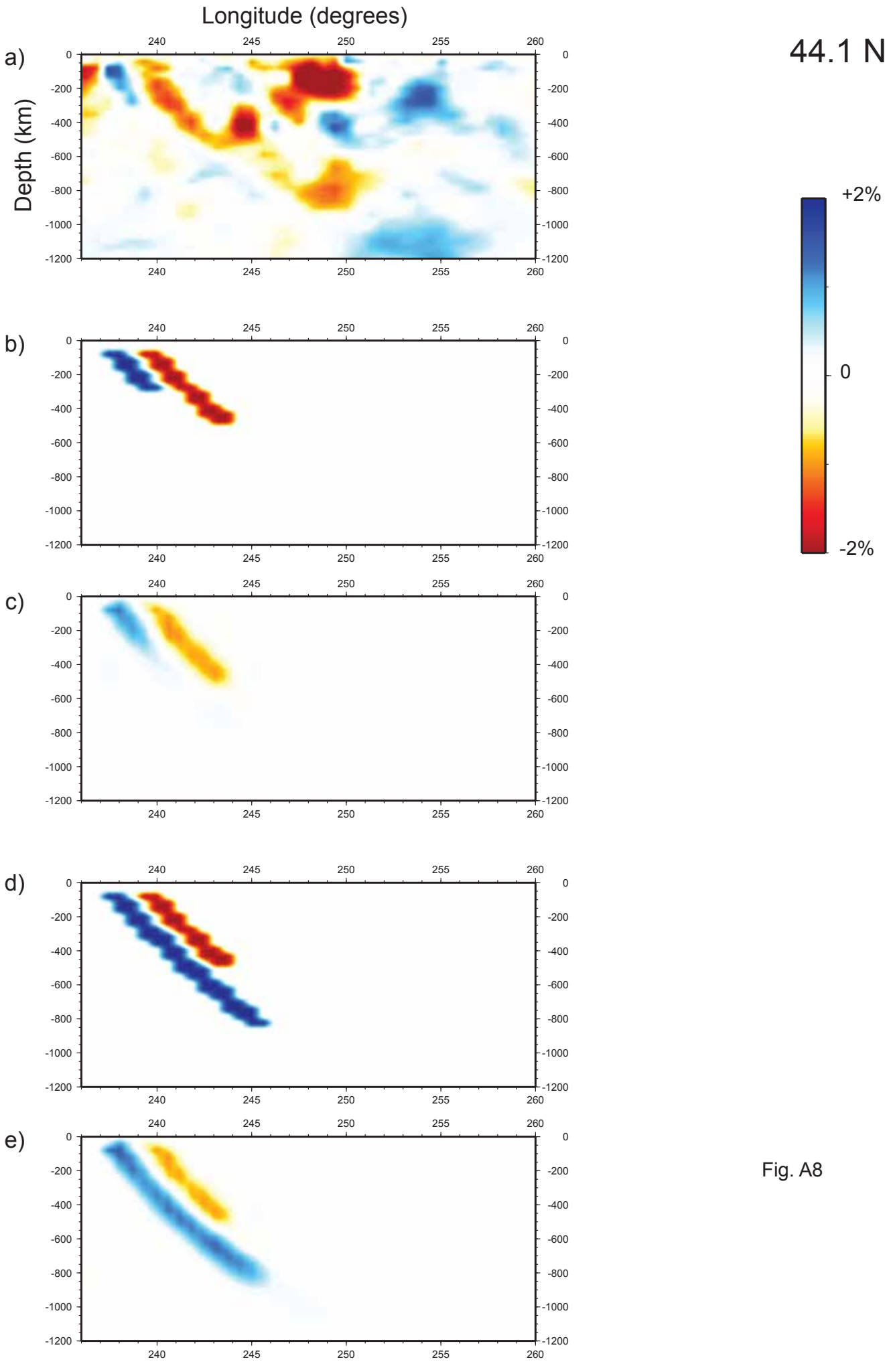
Longitude (degrees)
Depth (km)
a)
b)
c)
d)
e)
240
245
250
255
260
0
-200
-400
-600
-800
-1000
-1200
44.1 N
+2%
0
-2%

Fig. A8

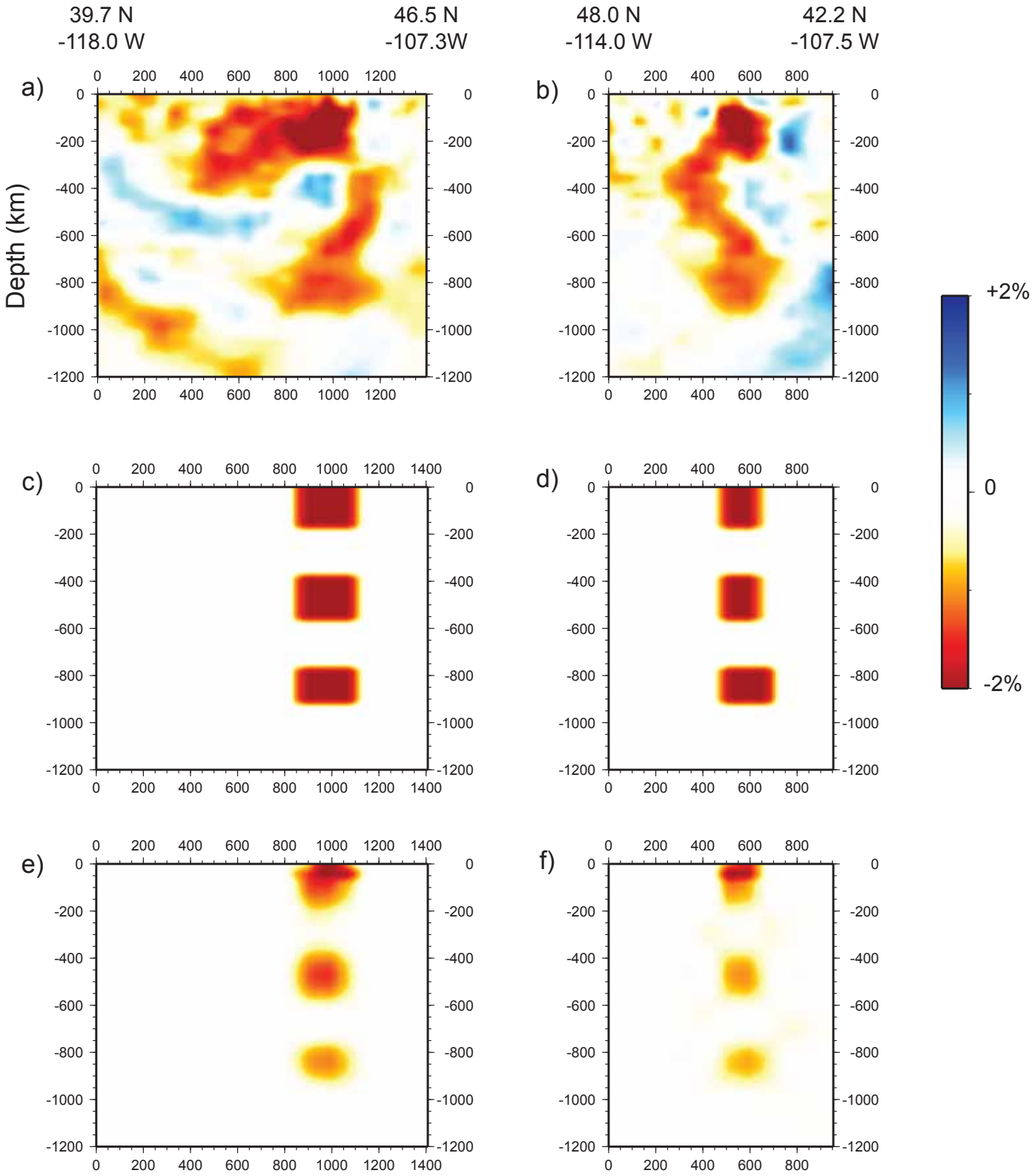
39.7 N
-118.0 W
46.5 N
-107.3W
48.0 N
-114.0 W
42.2 N
-107.5 W
a)
b)
c)
d)
e)
f)
Depth (km)
+2%
0
-2%

Fig. A9

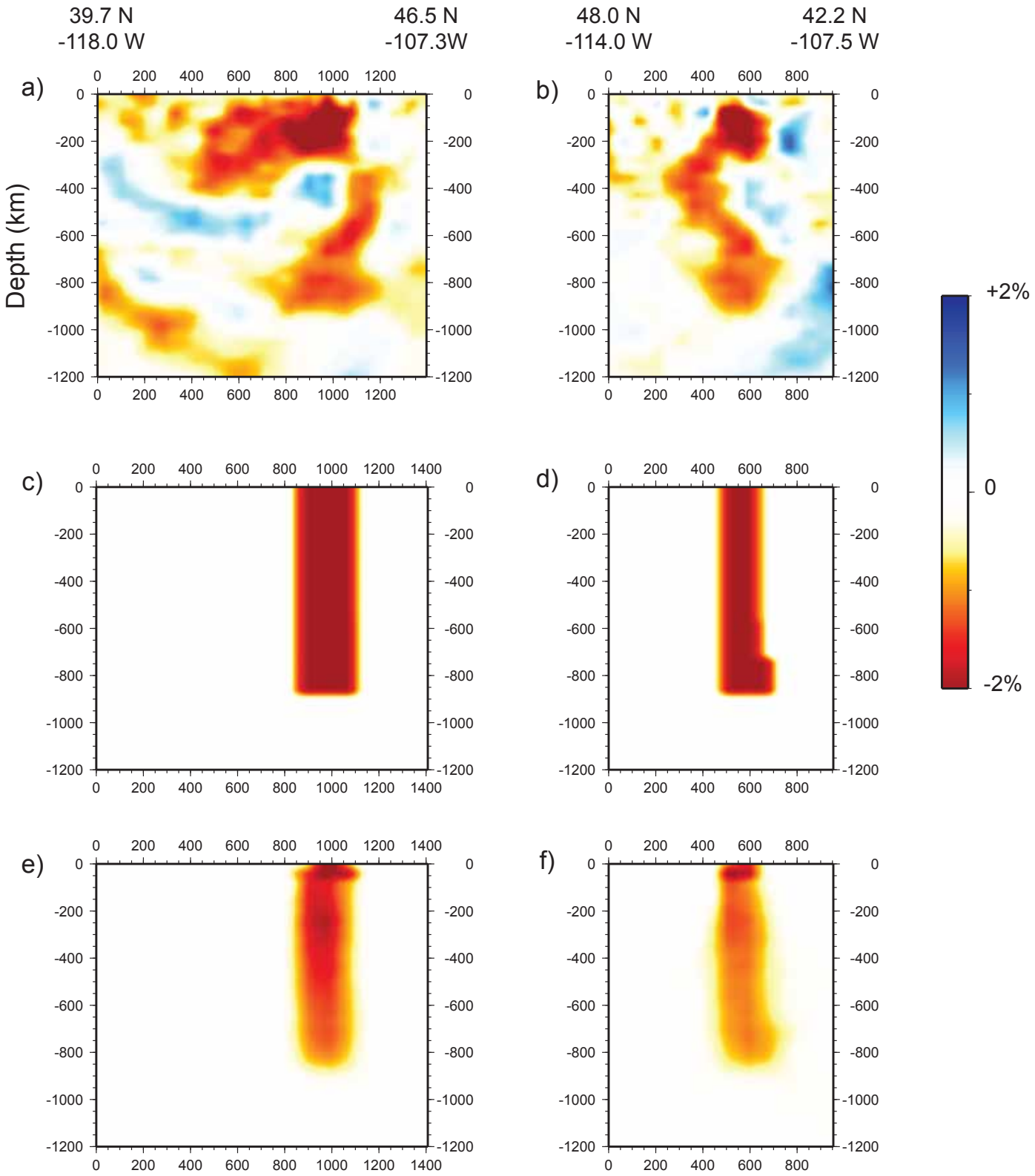
39.7 N
-118.0 W
46.5 N
-107.3W
48.0 N
-114.0 W
42.2 N
-107.5 W
a)
b)
c)
d)
e)
f)
Depth (km)
+2%
0
-2%

Fig. A10

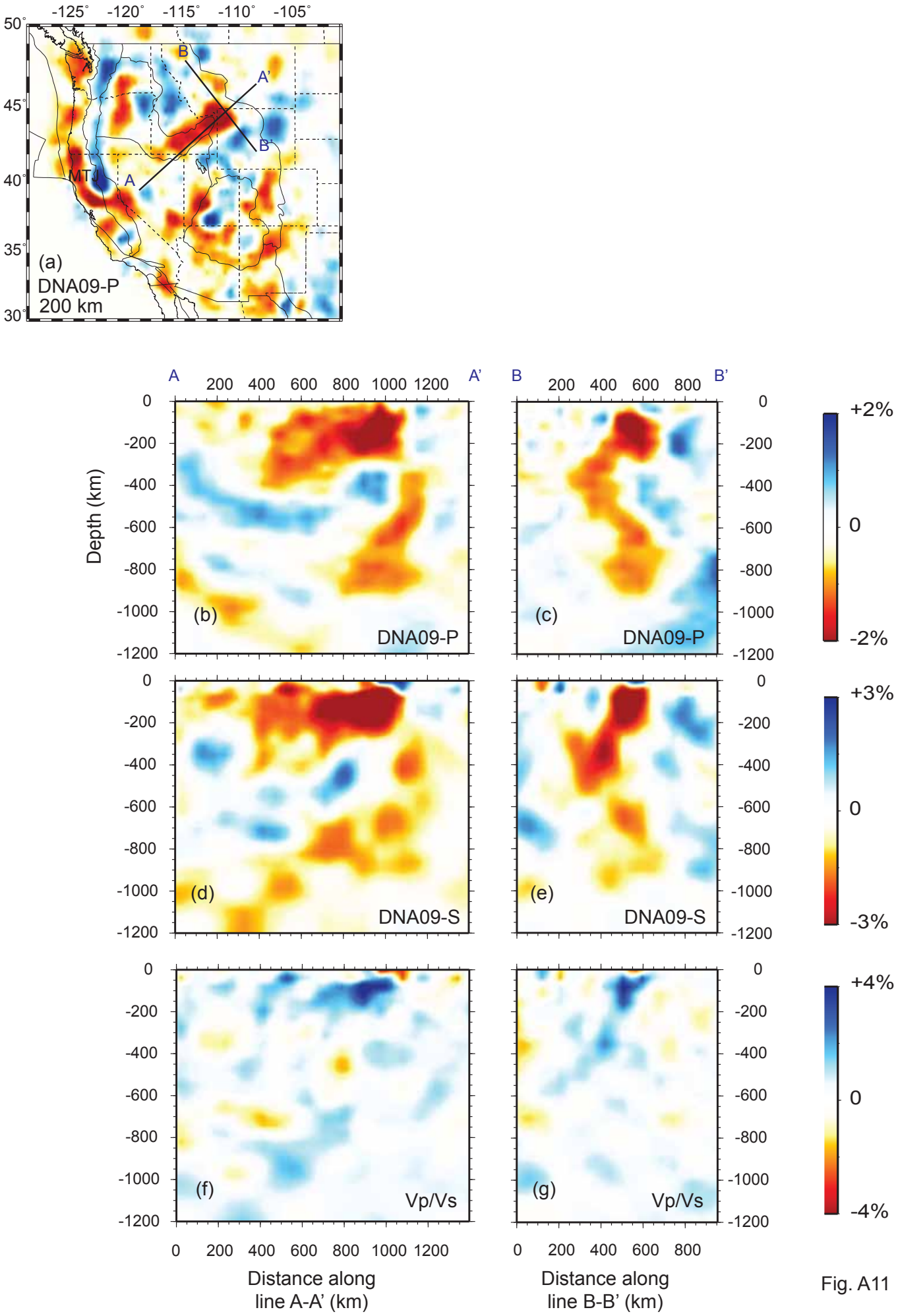
-125°
-120°
-115°
-110°
-105°
50°
45°
40°
35°
30°
B
A'
B'
A
MTJ
(a)
DNA09-P
200 km
A
A'
B
B'
Depth (km)
(b)
DNA09-P
(c)
DNA09-P
(d)
DNA09-S
(e)
DNA09-S
(f)
Vp/Vs
(g)
Vp/Vs
+2%
0
-2%
+3%
0
-3%
+4%
0
-4%
Distance along line A-A' (km)
Distance along line B-B' (km)

Fig. A11

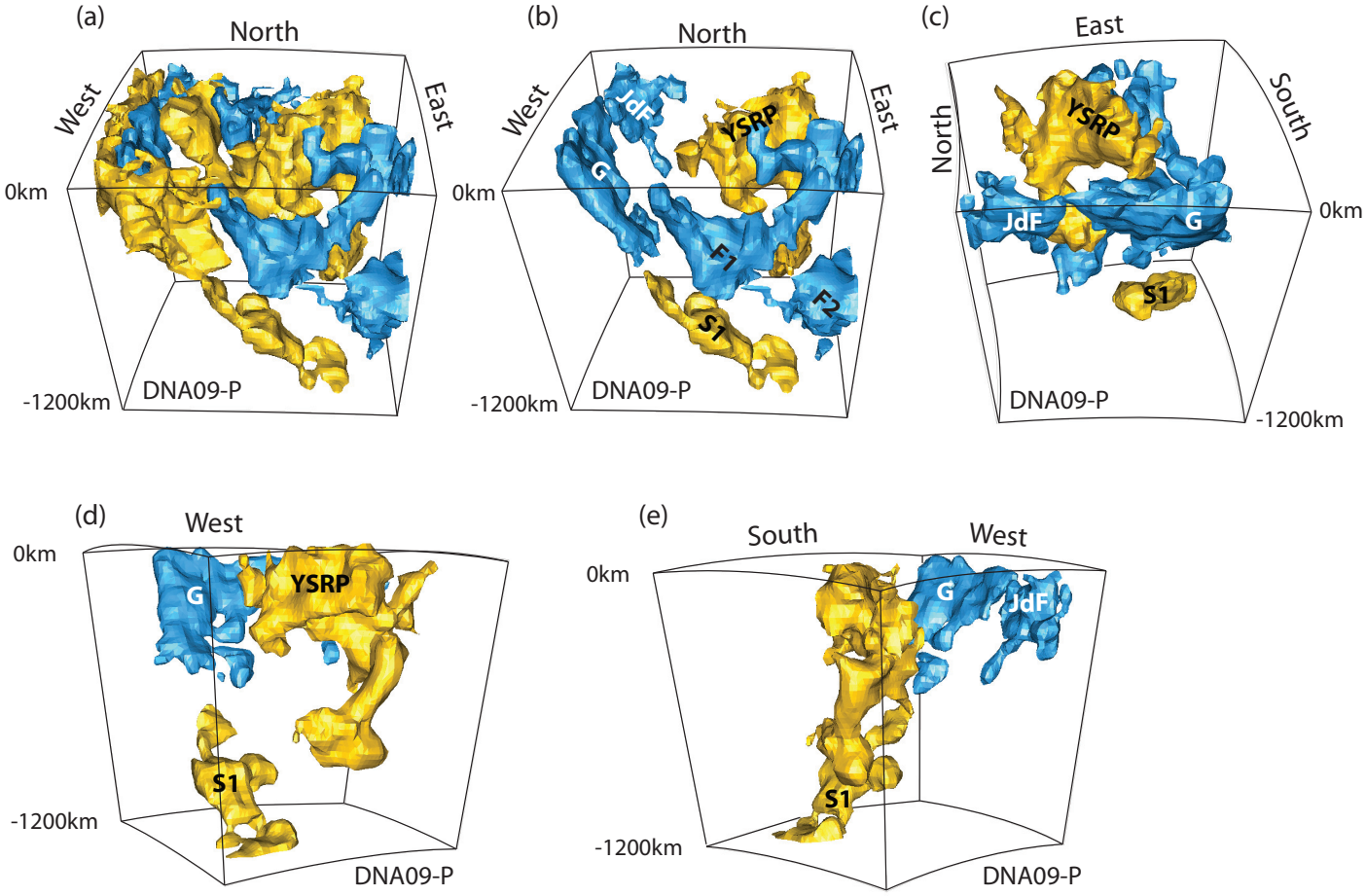
(a)
North
West
East
0km
-1200km
DNA09-P
(b)
North
West
East
JdF
YSRP
G
F1
F2
S1
0km
-1200km
DNA09-P
(c)
East
North
South
YSRP
JdF
G
S1
0km
DNA09-P
-1200km
(d)
West
0km
G
YSRP
S1
-1200km
DNA09-P
(e)
South
West
0km
G
JdF
S1
-1200km
DNA09-P

Fig. A12